A spectral boundary-integral method for quasi-dynamic ruptures of multiple parallel faults

Sylvain Barbot[1*]

[1]Department of Earth Sciences, University of Southern California,
3651 Trousdale Pkwy, Los Angeles, CA 90089, USA

*To whom correspondence should be addressed; E-mail: *sbarbot@usc.edu*

Abstract

Numerical models of rupture dynamics provide great insights into the physics of fault failure. However, resolving stress interactions among multiple faults remains challenging numerically. Here, we derive the elasto-static Green's functions for stress and displacement caused by arbitrary slip distributions along multiple parallel faults. The equations are derived in the Fourier domain, providing an efficient means to calculate stress interactions with the fast Fourier transform. We demonstrate the relevance of the method for a wide range of applications by simulating the rupture dynamics of single and multiple parallel faults controlled by a rate- and state-dependent frictional contact using the spectral boundary integral method and the radiation-damping approximation. Within the anti-plane strain approximation, we show seismic cycle simulations with a power-law distribution of rupture sizes and, in a different parameter regime, sequences of seismogenic slow-slip events. Using the in-plane strain approximation, we simulate the rupture dynamics of a restraining step-over. Finally, we describe cycles of large earthquakes along several parallel strike-slip faults in three-dimensions. The approach is useful to explore the dynamics of interacting or isolated faults with many degrees of freedom.

Key points

- We expand the spectral boundary integral method for fault modeling to multiple parallel faults.
- The method allows simulations of fault dynamics within step-overs and across distant faults.
- The approach enables seismic cycle simulations within a plate boundary fault network.

Introduction

The seismic phenomenon includes a wide variety of ruptures styles with slip velocities ranging from nanometers to meters per second (*Leeman et al.*, 2016; *Obara and Kato*, 2016). Deep insights into the physics of faulting has come from interconnected studies of natural outcrops, laboratory faults, seismo-geodetic remote sensing, and modeling. Numerical simulations of slow-slip events and seismogenic ruptures is complicated by the wide spectrum of spatial scales involved to resolve the rupture front, nucleation size, and seismic wave length on the one hand, and the overall dimension of the faults involved on the other (e.g., *Matsuzawa et al.*, 2010; *Barbot et al.*, 2012). Seismic cycles also involve a broad range of time scales, from seconds during dynamic rupture, to centuries during interseismic loading, to geological epochs during which the structural layout of plate boundaries takes shape (*Dinther et al.*, 2013; *Van Zelst et al.*, 2019).

Much effort has focused on simulations of single ruptures to better understand source processes, the characteristics of seismic waves, and how they may affect the built environment (e.g., *Madariaga*, 1976; *Andrews*, 1976). These simulations often rely on finite difference (*Day*, 1982; *Oglesby and Day*, 2002; *Kase and Day*, 2006; *Duan*, 2010), finite element (*Aagaard et al.*, 2001; *Oglesby and Archuleta*, 2003; *Tago et al.*, 2012; *Aagaard et al.*, 2013; *Rezakhani et al.*, 2020), or spectral element (*Puente et al.*, 2009; *Pelties et al.*, 2012; *Gabriel et al.*, 2012) methods with internal boundaries representing faults. The maturity and versatility of these volume methods afford geometrically complex ruptures spanning several fault branches (*Uphoff et al.*, 2017; *Wollherr et al.*, 2019; *Ulrich et al.*, 2019), but the associated computational burden makes simulations of long sequences of ruptures challenging (e.g., *Duan and Oglesby*, 2005; *Luo et al.*, 2020), unless within a two-dimensional approximation (*Kaneko et al.*, 2008; *Ma et al.*, 2019; *Thakur et al.*, 2020).

The boundary integral method provides an efficient means to incorporate complex fault geometry as only the fault interface must be discretized numerically, the bulk elastic behavior being captured by analytic Green's functions (e.g., *Aochi and Fukuyama*, 2002; *Bhat et al.*, 2007; *Ando and Kaneko*, 2018; *Noda et al.*, 2020). The boundary integral method may capture wave-mediated stress transfer (e.g., *Andrews*, 1985; *Bouchon et al.*, 1989; *Chen and Zhang*, 2006; *Otani et al.*, 2007; *Tada*, 2009; *Ando*, 2016) or operate under the quasi-dynamics approximation (*Tse and Rice*, 1986; *Rice*, 1993; *Liu and Rice*, 2005; *Liu et al.*, 2012; *Dublanchet et al.*, 2013; *Ong et al.*, 2019; *Barbot*, 2019b). The integral method may also be extended to represent plastic deformation in the bulk (*Kato*, 2002; *Lambert and Barbot*, 2016; *Barbot*, 2018b, 2020a; *Shi et al.*, 2020), thermo-mechanical effects (*Noda and Lapusta*, 2010; *Wang and Barbot*, 2020), or localized deformation associated with folding (*Sathiakumar et al.*, 2020). Currently, many flavors of Green's functions are used based on rectangle (*Fukuyama and Madariaga*, 2000), triangle (*Li and Liu*, 2016, 2017), and other polygonal surface elements (*Hori and Miyazaki*, 2011; *Ohtani et al.*, 2014) conforming to planar and curvilinear faults. However, resolving the stress evolution in mechanical systems with many degrees of freedom remains challenging because the number of interactions increases algebraically. Technical improvements on the boundary integral method for better numerical efficiency include the hierarchical matrix (*Bradley*, 2014) and the fast multipole (*Romanet et al.*, 2018) methods, but geophysical applications have been limited.

A leap in numerical efficiency that enables modeling large faults comes from the spectral boundary integral method, whereby the stress interactions are evaluated in the Fourier domain (*Geubelle and Rice*, 1995; *Perrin et al.*, 1995; *Bouchon and Streiff*, 1997; *Lapusta et al.*, 2000; *Gallovič*, 2008; *Lapusta and Liu*, 2009; *Dublanchet*, 2019). The appeal of the method hinges on the algorithmic efficiency of the fast Fourier transform that reduces the numerical complexity from $\mathcal{O}(N^2)$ to $\mathcal{O}(N \log N)$, where N is the system size. However, the approach is limited to planar fault geometry. The spectral boundary integral method has made possible many studies of fault dynamics that resolve all phases of the seismic cycle on finite faults (e.g., *Lapusta and Rice*, 2003; *Chen and Lapusta*, 2009; *Barbot et al.*, 2012; *Lapusta and Barbot*, 2012; *Jiang and Lapusta*, 2016; *Dublanchet*, 2020) including slow-slip events (*Veedu and Barbot*, 2016; *Veedu et al.*, 2020; *Dal Zilio et al.*, 2020).

While an important control of fault dynamics is wave-mediated stress transfer, the effect of seismic waves can be neglected in many problems of fundamental interest in geophysics, for example, creep waves, afterslip, slow-slip events, and earthquake nucleation. In addition, some problems are so numerically demanding that including seismic waves is still impractical, for example faults with a velocity-weakening region that dramatically outsizes the nucleation size (*Lapusta and Rice*, 2003; *Wu and Chen*, 2014; *Barbot*, 2019b; *Cattania*, 2019) or faults with large aspect ratios. The radiation damping approximation should be employed in these cases (*Rice*, 1993), with well-understood caveats (*Thomas et al.*, 2014).

To expand the range of application of the spectral boundary integral method, we develop the elasto-static Green's functions for multiple-parallel faults in two and three-dimensional media. We take the novel approach of directly Fourier-transforming the space-domain elasto-static Green's functions, providing the closed-form solutions for the displacement and stress along parallel planes in the Fourier domain. The approach is still limited to planar faults, but there may be arbitrarily many faults, possibly offset along-strike. Considering planar faults makes the fast Fourier transform applicable, maintaining the numerical efficiency of the spectral boundary integral method, but relaxing the limitation of a single fault plane.

In the next section, we derive the Green's function for stress interactions in the Fourier domain for a three-dimensional unbounded space, starting with the representation theorem for a dislocation of finite size. Although we do not discuss this further, the solution for a half-space for vertical faults may be approximated using the method of images. We then derive the Fourier-domain solution for the anti-plane and in-plane strain two-dimensional cases, starting with the respective space-domain Green's functions. In the following section, we illustrate the efficiency of the approach by simulating seismic cycle simulations in numerically challenging cases. We use the anti-plane strain approximation to simulate long sequences of ruptures that exhibit a quasi power-law distribution of seismic moment across four orders of magnitude. We then illustrate the emergence of seismogenic slow-slip events whereby the underlying slow rupture is interspersed with numerous small seismic events. Next, we use the in-plane strain setup to simulate the dynamics of a restraining fault step-over involving two fault branches. Finally, we consider the case of finite faults in a three-dimensional medium by simulating the interaction of four parallel strike-slip faults with a separation distance of the order of crustal depth, a layout typical of the termination of large continental transform faults. The proposed approach may be useful to simulate seismic cycles on single and multiple interacting faults involving many degrees of freedom.

Fourier-domain Green's functions

Analytic Green's functions afford efficient ways to connect source processes to observations and *vice-versa* without numerical sampling of the intervening space (e.g., *Okada*, 1992; *Bouchon and Sánchez-Sesma*, 2007; *Barbot*, 2018a). Fourier-domain Green's functions constitute a subset where the interaction can be described by a transfer function between source and receivers. While the range of applicability is reduced, the advantage is a dramatically faster computation, which has been exploited in many areas of crustal dynamics (*Steketee*, 1958; *Sato and Matsu'ura*, 1973; *Wang et al.*, 2003; *Smith and Sandwell*, 2004; *Fukahata and Matsu'ura*, 2005; *Wang et al.*, 2006; *Barbot et al.*, 2009; *Barbot and Fialko*, 2010; *Barbot et al.*, 2017).

A classical approach for deriving Fourier-domain Green's functions in elasticity has been to solve the governing equation for any wavenumber, involving propagator matrices (*Gilbert and Backus*, 1966; *Pan*, 2019). We take an alternative approach where we directly Fourier-transform the space-domain Green's function. This allows for a simpler derivation involving only scalar quantities. We start by deriving the Fourier-domain Green's functions for a three-dimensional space, then derive simpler expressions for the two-dimensional cases of anti-plane and in-plane strain.

Three-dimensional formulation

We consider a full elastic space cut by an internal boundary representing a fault plane. We define a right-handed orthonormal reference system centered on the fault where the basis vectors $\mathbf{e}_1$ and $\mathbf{e}_2$ are fault-parallel and the remaining vector $\mathbf{e}_3$ is fault-perpendicular (Figure 1). We seek to express the stress field in the elastic medium due to an arbitrary slip distribution on the fault plane, where slip is defined as a displacement discontinuity. For this derivation, we consider only one fault plane, as the solution for multiple ones can be obtained by linear superposition.

We associate slip on the fault with a distribution of plastic strain

$$\boldsymbol{\epsilon}^i = \frac{1}{2}\left(\mathbf{s}\otimes\mathbf{e}_3 + \mathbf{e}_3\otimes\mathbf{s}\right) \;, \tag{1}$$

where $\mathbf{s}$ is the slip distribution and $\otimes$ represent the dyadic product between vectors. We only consider the case of shear cracks, for which we have $\mathbf{s} = s_1\,\mathbf{e}_1 + s_2\,\mathbf{e}_2$. We consider the slip distribution a function of three-dimensional space, with $s_i(\mathbf{x}) = s_i(x_1, x_2)\,\delta(x_3)$, for $i = 1, 2$, where $\delta(x)$ is the delta function.

We invoke the representation theorem of elasticity (e.g., *Aki and Richards*, 1980, Chapter 3) that associates any deviatoric plastic strain with the distribution of equivalent body-force $\mathbf{f} = -2\mu\,\nabla\cdot\boldsymbol{\epsilon}^i$, where μ is the shear modulus (*Barbot*, 2018a). Using the plastic strain of equation (1) leads to

$$\begin{aligned}\mathbf{f} = -\mu\Big[& s_1\,\delta_{,3}(x_3)\,\mathbf{e}_1 + s_2\,\delta_{,3}(x_3)\,\mathbf{e}_2 \\ & + (s_{1,1}+s_{2,2})\,\delta(x_3)\,\mathbf{e}_3\Big] \;,\end{aligned} \tag{2}$$

where the comma subscript represents differentiation. The terms with the derivative of delta functions correspond to fault-parallel force couples and the terms with delta functions are the double couples in the fault-perpendicular direction. The displacement field is obtained by a convolution with the elasto-static Green's functions, expressed as

$$u_i = \int_\Omega g_{ji}(\mathbf{x}-\mathbf{y}) f_j(\mathbf{y})\,\mathrm{d}\mathbf{y} \;, \tag{3}$$

where Einstein's summation convention is used and the components of the Green's function tensor are given by

$$g_{ij} = \frac{1}{8\pi\mu}\left[(2-\alpha)\frac{1}{R}\delta_{ij} + \alpha\frac{r_i r_j}{R^3}\right] \;, \tag{4}$$

where

$$\alpha = \frac{1}{2(1-\nu)} = \frac{\lambda+\mu}{\lambda+2\mu} \tag{5}$$

is an elastic constant depending on the Lamé parameters λ and μ and $r_i = x_i - y_i$. The radial distance from a source is defined as $R^2 = (x_k - y_k)(x_k - y_k)$ using Einstein's summation convention. We consider the two-dimensional Fourier transform defined by the integral

$$\hat{f}(k_1, k_2) = \iint_{-\infty}^{\infty} f(x_1, x_2)\, e^{-i2\pi(k_1 x_1 + k_2 x_2)}\,\mathrm{d}x_1\mathrm{d}x_2 \;, \tag{6}$$

where k_1 and k_2 are the wavenumbers in the directions parallel to $\mathbf{e}_1$ and $\mathbf{e}_2$, respectively, and we use the notation $\hat{f} = \mathcal{F}[f]$ to denote the corresponding two-dimensional integral transform. We also introduce the notations $\omega_1 = 2\pi k_1$, $\omega_2 = 2\pi k_2$, and $\omega = {\omega_1}^2 + {\omega_2}^2$ to simplify the following expressions.

We seek to evaluate the convolution in the Fourier domain, taking advantage of the convolution theorem of the Fourier transform. The displacement field can be obtained by conducting several convolutions, specifically

$$\begin{aligned}\frac{1}{\mu}u_i(\mathbf{x}) = & -\iiint_{-\infty}^{\infty} g_{1i}(\mathbf{x}-\mathbf{y})\, s_1(y_1, y_2)\,\frac{\partial\delta(y_3)}{\partial y_3}\,\mathrm{d}\mathbf{y} \\ & -\iiint_{-\infty}^{\infty} g_{1i}(\mathbf{x}-\mathbf{y})\, s_2(y_1, y_2)\,\frac{\partial\delta(y_3)}{\partial y_3}\,\mathrm{d}\mathbf{y} \\ & -\iiint_{-\infty}^{\infty} g_{3i}(\mathbf{x}-\mathbf{y}) s_{1,1}(y_1, y_2)\delta(y_3)\,\mathrm{d}\mathbf{y} \\ & -\iiint_{-\infty}^{\infty} g_{3i}(\mathbf{x}-\mathbf{y}) s_{2,2}(y_1, y_2)\delta(y_3)\,\mathrm{d}\mathbf{y} \;.\end{aligned} \tag{7}$$

Making use of the properties of the delta function, the convolution theorem, and other common properties of the Fourier transform, the displacement field in the Fourier domain simplifies to

$$\begin{aligned}\frac{1}{\mu}\hat{u}_i(k_1,k_2,x_3) =& \frac{\partial}{\partial y_3}\left\{\mathcal{F}\left[g_{1i}\right]\right\}\Big|_{,y_3=0}\hat{s}_1 \\ &+\frac{\partial}{\partial y_3}\left\{\mathcal{F}\left[g_{2i}\right]\right\}\Big|_{,y_3=0}\hat{s}_2 \\ &-\mathcal{F}\left[g_{3i}\right]\Big|_{,y_3=0}\left(i\omega_1\hat{s}_1+i\omega_2\hat{s}_2\right)\ .\end{aligned} \tag{8}$$

We are left to express the Fourier transforms of the Green's function components to find the closed-form solution.

We first derive a result that, if not important on its own, will be useful for the following developments. Consider the Green's function of the three-dimensional harmonic equation, i.e., the solution to $\nabla^2 f(\mathbf{x}) = \delta(\mathbf{x})$ given by

$$f(\mathbf{x}) = -\frac{1}{4\pi R}\ , \tag{9}$$

which is obtained by integrating twice in spherical coordinates. Consider the same harmonic equation, but after a two-dimensional Fourier transform, given by

$$\left[\frac{\partial^2}{\partial {x_3}^2}-\omega^2\right]\hat{f}(x_3) = \delta(x_3)\ . \tag{10}$$

The solution can be obtained by the method of variation of parameters, considering the radiation condition at distant $x_3 \geq 0$, to get

$$\begin{aligned}\hat{f}(x_3) &= -\frac{1}{2\omega}\left\{\int_{-\infty}^{\infty} e^{\omega x_3}\delta(x_3)\mathrm{d}x_3\right\}e^{-\omega x_3} \\ &= -\frac{1}{2\omega}e^{-\omega x_3}\ .\end{aligned} \tag{11}$$

Then, considering the properties of the Fourier transform with respect to differentiation and integration, we obtain the following key results

$$\begin{aligned}\mathcal{F}\left[\frac{1}{R}\right] &= 2\pi\frac{1}{w}\,e^{-\omega r_3}\ , \\ \mathcal{F}\left[\frac{r_1}{R^3}\right] &= -i2\pi\frac{\omega_1}{w}\,e^{-\omega r_3}\ , \\ \mathcal{F}\left[\frac{r_1^2}{R^3}\right] &= 2\pi\frac{{\omega_2}^2-{\omega_1}^2\omega r_3}{w^3}\,e^{-\omega r_3}\ , \\ \mathcal{F}\left[\frac{r_1 r_2}{R^3}\right] &= -2\pi\frac{\omega_1\omega_2}{\omega^3}(1+\omega r_3)\,e^{-\omega r_3}\ ,\end{aligned} \tag{12}$$

for $r_3 \geq 0$. Some components of the Green's function constitute linear combinations of the above terms and their derivatives. Others can be derived in a similar manner by substituting the indices 1 and 2.

Let us consider the displacement component

$$\begin{aligned}\frac{1}{\mu}\hat{u}_1 =& \frac{\partial}{\partial y_3}\left\{\mathcal{F}\left[g_{11}\right]\right\}\Big|_{y_3=0}\hat{s}_1 \\ &+\frac{\partial}{\partial y_3}\left\{\mathcal{F}\left[g_{21}\right]\right\}\Big|_{y_3=0}\hat{s}_2 \\ &-\mathcal{F}\left[g_{31}\right]\Big|_{y_3=0}\left(i\omega_1\hat{s}_1+i\omega_2\hat{s}_2\right)\end{aligned} \tag{13}$$

with the Green's function components

$$
\begin{aligned}
\mu g_{11} &= \frac{1}{8\pi}\left[(2-\alpha)\frac{1}{R}+\alpha\frac{{r_1}^2}{R^3}\right] \ , \\
\mu g_{21} &= \frac{\alpha}{8\pi}\,\frac{r_1 r_2}{R^3} \ , \\
\mu g_{31} &= \frac{\alpha}{8\pi}\,\frac{r_1 r_3}{R^3} \ .
\end{aligned}
\tag{14}
$$

Exploiting the results of equation (12), we obtain

$$
\begin{aligned}
\mu\,\frac{\partial}{\partial y_3}\left\{\mathcal{F}\left[g_{11}\right]\right\}_{\big|y_3=0} &= \frac{1}{4\omega}\left[2\omega-\alpha x_3{\omega_1}^2\right]e^{-\omega x_3} \ , \\
\mu\,\frac{\partial}{\partial y_3}\left\{\mathcal{F}\left[g_{21}\right]\right\}_{\big|y_3=0} &= -\frac{\alpha}{4\omega}\omega_1\omega_2 x_3\,e^{-\omega x_3} \ , \\
-i\mu\,\mathcal{F}\left[g_{31}\right]_{\big|y_3=0} &= -\frac{\alpha}{4\omega}\omega_1 x_3\,e^{-\omega x_3} \ .
\end{aligned}
\tag{15}
$$

Collecting the terms, we obtain the displacement components

$$
\begin{aligned}
\hat{u}_1 &= \frac{-1}{2\omega}\left\{\left[\alpha\omega_1^2 x_3-\omega\right]\hat{s}_1+\alpha\omega_1\omega_2 x_3\,\hat{s}_2\right\}e^{-\omega x_3} \\
\hat{u}_2 &= \frac{-1}{2\omega}\left\{\alpha\omega_1\omega_2 x_3\,\hat{s}_1+\left[\alpha\omega_2^2 x_3-\omega\right]\hat{s}_2\right\}e^{-\omega x_3} \ ,
\end{aligned}
\tag{16}
$$

where the solution for $\hat{u}_2$ has been obtained by exploiting the symmetry of the problem, simply permuting the indices 1 and 2.

We now consider the remaining component of displacement

$$
\begin{aligned}
\frac{1}{\mu}\hat{u}_3 =& \frac{\partial}{\partial y_3}\left\{\mathcal{F}\left[g_{13}\right]\right\}_{\big|y_3=0}\hat{s}_1 \\
&+\frac{\partial}{\partial y_3}\left\{\mathcal{F}\left[g_{23}\right]\right\}_{\big|y_3=0}\hat{s}_2 \\
&-\mathcal{F}\left[g_{33}\right]_{\big|y_3=0}\left(i\omega_1\hat{s}_1+i\omega_2\hat{s}_2\right) \ ,
\end{aligned}
\tag{17}
$$

with the Green's function components

$$
\begin{aligned}
\mu g_{13} &= \frac{\alpha}{8\pi}\,\frac{r_1 r_3}{R^3} \ . \\
\mu g_{23} &= \frac{\alpha}{8\pi}\,\frac{r_2 r_3}{R^3} \ , \\
\mu g_{33} &= \frac{1}{8\pi}\left[(2-\alpha)\frac{1}{R}+\alpha\frac{{r_3}^2}{R^3}\right] \ .
\end{aligned}
\tag{18}
$$

Deriving the following results by considering equation (12)

$$
\begin{aligned}
\mu\,\frac{\partial}{\partial y_3}\left\{\mathcal{F}\left[g_{13}\right]\right\}_{\big|y_3=0} &= -\frac{\alpha}{4\omega}i\omega_1(\omega x_3-1)e^{-\omega x_3} \\
\mu\,\frac{\partial}{\partial y_3}\left\{\mathcal{F}\left[g_{23}\right]\right\}_{\big|y_3=0} &= -\frac{\alpha}{4\omega}i\omega_2(\omega x_3-1)\,e^{-\omega x_3} \\
-i\mu\,\left\{\mathcal{F}\left[g_{31}\right]\right\}_{\big|y_3=0} &= -\frac{\alpha}{4\omega}\omega_1 x_3\,e^{-\omega x_3} \ ,
\end{aligned}
\tag{19}
$$

we obtain the fault-perpendicular displacement component

$$
\begin{aligned}
\hat{u}_3 = \frac{-i}{2\omega}\{ & \left[(1-\alpha)\omega_1 + \alpha\omega_1\omega x_3\right]\hat{s}_1 \\
& + \left[(1-\alpha)\omega_2 + \alpha\omega_2\omega x_3\right]\hat{s}_2\} e^{-\omega x_3} \ .
\end{aligned}
\tag{20}
$$

The solution displacement so far only considered $x_3 \geq 0$ to simplify the treatment. The solution for the whole space can be obtained by considering the symmetry of displacement with regard to a planar dislocation. Fault-parallel displacement must be anti-symmetric with respect to the fault plane, such that u_1 and u_2 are odd functions of x_3. In contrast, fault-perpendicular displacements must be symmetric with respect to the fault plane, such that u_3 is an even function of x_3. In addition, the displacement field must decay exponentially on both sides of the fault. This provides us with the full space solution displacement

$$
\begin{aligned}
\hat{u}_1 &= \frac{-1}{2\omega}\Bigg\{ \left[\alpha\omega_1^2 x_3 - \operatorname{sign}(x_3)\,\omega\right]\hat{s}_1 \\
&\qquad + \alpha\omega_1\omega_2 x_3\,\hat{s}_2 \Bigg\} e^{-\omega|x_3|} \\
\hat{u}_2 &= \frac{-1}{2\omega}\Bigg\{ \alpha\omega_1\omega_2 x_3\,\hat{s}_1 \\
&\qquad + \left[\alpha\omega_2^2 x_3 - \operatorname{sign}(x_3)\,\omega\right]\hat{s}_2 \Bigg\} e^{-\omega|x_3|} \ , \\
\hat{u}_3 &= \frac{-i}{2\omega}\Bigg\{ \left[(1-\alpha) + \alpha\omega|x_3|\right]\omega_1\hat{s}_1 \\
&\qquad + \left[(1-\alpha) + \alpha\omega|x_3|\right]\omega_2\hat{s}_2 \Bigg\} e^{-\omega|x_3|} \ ,
\end{aligned}
\tag{21}
$$

where we used the function $\operatorname{sign}(x)$ for the sign of x_3. The relevant stress components that affect the traction on parallel faults are obtained by linear combinations of derivatives of displacement, following Hooke's law for an isotropic elastic material, with $\sigma_{ij} = \lambda u_{k,k}\delta_{ij} + \mu(u_{i,j} + u_{j,i})$, where δ_{ij} is the Kronecker delta. After some algebra, they simplify to

$$
\begin{aligned}
\hat{\sigma}_{13} &= \frac{-\mu}{2\omega}\Bigg\{ \left[{\omega_2}^2 + 2\alpha{\omega_1}^2(1-\omega|x_3|)\right]\hat{s}_1 \\
&\qquad + \left[(2\alpha-1) - 2\alpha\omega|x_3|\right]\omega_1\omega_2\,\hat{s}_2 \Bigg\} e^{-\omega|x_3|} \\
\hat{\sigma}_{23} &= \frac{-\mu}{2\omega}\Bigg\{ \left[(2\alpha-1) - 2\alpha\omega|x_3|\right]\omega_1\omega_2\,\hat{s}_1 \\
&\qquad + \left[{\omega_1}^2 + 2\alpha{\omega_2}^2(1-\omega|x_3|)\right]\hat{s}_2 \Bigg\} e^{-\omega|x_3|} \\
\hat{\sigma}_{33} &= \mu\,\alpha\,\omega x_3\,(i\omega_1\hat{s}_1 + i\omega_2\hat{s}_2)\,e^{-\omega|x_3|} \ ,
\end{aligned}
\tag{22}
$$

where, because of the symmetry about the fault plane, σ_{13} and σ_{23} are even functions of x_3 and σ_{33} is an odd function of x_3. The components $\hat{\sigma}_{13}$ and $\hat{\sigma}_{23}$ can be obtained from each other by permutation of the indices 1 and 2. The change of confining stress, an odd function of x_3,

$$
\frac{1}{3}\sigma_{kk} = \mu\frac{4\alpha-1}{3}\operatorname{sign}(x_3)\,(i\omega_1\hat{s}_1 + i\omega_2\hat{s}_2)\,e^{-\omega|x_3|}
\tag{23}
$$

may also be of interest. Along the fault, the traction components simplify to

$$
\begin{aligned}
\hat{\sigma}_{13} &= \frac{-\mu}{2\omega}\left[\left({\omega_2}^2+2\alpha{\omega_1}^2\right)\hat{s}_1+(2\alpha-1)\omega_1\omega_2\,\hat{s}_2\right] \\
\hat{\sigma}_{23} &= \frac{-\mu}{2\omega}\left[(2\alpha-1)\omega_1\omega_2\,\hat{s}_1+\left({\omega_1}^2+2\alpha{\omega_2}^2\right)\hat{s}_2\right] \\
\hat{\sigma}_{33} &= 0\ ,
\end{aligned}
\tag{24}
$$

which is the result described by *Geubelle and Rice* (1995) and (*Lapusta and Liu*, 2009, Equation 5). Other stress components do not affect the traction on any parallel fault and are ignored.

The displacement and stress components of equation (21) and (22) are shown in the Supplementary Materials for the case of a uniform distribution of slip in the x_1 direction within a 4×4 km square patch. The displacement and stress are calculated at a distance $x_3 = 2$ km from the fault. As the Fourier-domain solution is not defined at the $\omega = 0$ wavenumber without further information, we assume zero mean displacement and zero mean stress. The displacement field shows the typical convergence and divergence pattern near the fault tips with compressional deformation in the compressional quadrant. However, the change of normal stress is only subtle.

We compare the Fourier-domain solutions with the corresponding analytic solution (*Okada*, 1992) for the case of dip-slip motion (Supplementary Materials). The comparison reveals major differences due to the periodicity of the discrete Fourier transform and the assumption of zero mean stress, with long-wavelength residuals emanating from the four corners for the σ_{13} component and more widely distributed residuals for the σ_{23} component. These differences decay with increasing domain size, but remain within a few percents for realistic domain sizes in practical applications, which is typical for Fourier-domain solutions of elasto-static problems (*Barbot and Fialko*, 2010). These differences highlight that the discrete Fourier-domain and space-domain formulations are solutions to problems with different boundary conditions.

Anti-plane strain stress interaction

We now consider cases where variations along a given direction can be neglected, starting with anti-plane strain, which is relevant for long faults with strike-slip motion. We assume that derivatives with respect to x_1 can be neglected and that fault slip can be written as $\mathbf{s}(\mathbf{x}) = s_1(x_2)\,\delta(x_3)\,\mathbf{e}_1$. The equivalent body-force simplifies to

$$
\mathbf{f}(\mathbf{x}) = -\mu\, s_1(x_2)\frac{\partial\delta(x_3)}{\partial x_3}\mathbf{e}_1\ , \tag{25}
$$

and the governing equation reduces to Poisson's equation, following

$$
\nabla^2 u_1(x_2,x_3) + f_1(x_2,x_3) = 0\ . \tag{26}
$$

The solution displacement can be obtained by convolution with the Green's function

$$
\begin{aligned}
u_1(\mathbf{x}) &= \iint_{-\infty}^{\infty} g_{11}(\mathbf{x}-\mathbf{y})f_1(\mathbf{y})\,\mathrm{d}\mathbf{y} \\
&= \mu\int_{-\infty}^{\infty}\frac{\partial}{\partial y_3}\Big\{g_{11}(\mathbf{x}-\mathbf{y})\Big\}_{|y_3=0} s_1(y_2)\,\mathrm{d}y_2\ ,
\end{aligned}
\tag{27}
$$

with the Green's function tensor component

$$
g_{11} = \frac{-1}{2\pi\mu}\ln R\ , \tag{28}
$$

with $R^2 = (x_2 - y_2)^2 + (x_3 - y_3)^2$. However, we seek a closed-form solution of equation (26) in the Fourier domain, considering the one-dimensional Fourier transform

$$\hat{f}(k_2) = \int_{-\infty}^{\infty} f(x_2)\, e^{-i2\pi k_2 x_2}\, \mathrm{d}x_2 \ . \tag{29}$$

Applying the convolution theorem of the Fourier transform, the solution can be expressed as

$$\hat{u}_1(k_2, x_3) = \mu \frac{\partial}{\partial y_3} \Big\{ \mathcal{F}[g_{11}] \Big\}_{\big| y_3 = 0} \hat{s}_1 \ , \tag{30}$$

and we are left with identifying the Fourier transform of the Green's function component g_{11}.

Before we proceed with the derivation, we describe a general result for Poisson's equation

$$\nabla^2 f = \delta(x_2, x_3) \tag{31}$$

that will be useful for two-dimensional problems in this and the next section. The solution to equation (31) can be obtained by integrating twice in a cylindrical coordinate system and by taking advantage of the special properties of the delta function, to arrive at

$$f(x_2, x_3) = \frac{1}{2\pi} \ln R \ , \tag{32}$$

where $R^2 = {x_2}^2 + {x_3}^2$. After a one-dimensional Fourier transform, Poisson's equation can also be written

$$\left[\frac{\partial^2}{\partial {x_3}^2} - {\omega_2}^2 \right] \hat{f} = \delta(x_3) \ . \tag{33}$$

As in the previous section, the solution can be obtained by the method of variation of parameters, as follows

$$\begin{aligned} \hat{f}(x_3) &= -\frac{e^{-\omega_2 x_3}}{2\omega_2} \int e^{\omega_2 x_3} \delta(x_3) \mathrm{d}x_3 \\ &= -\frac{1}{2\omega_2} e^{-\omega_2 x_3} \ , \end{aligned} \tag{34}$$

for $x_3 \geq 0$ and $\omega_2 \geq 0$. We only consider the case of $\omega_2 \geq 0$ because only the positive part of the spectrum is sampled in real-to-complex and complex-to-real discrete Fourier transforms in numerically efficient applications. The extension of (34) and subsequent equations to the negative side of the spectrum is simply the complex conjugate, e.g., $\hat{f}(-\omega_2) = \overline{\hat{f}(\omega_2)}$.

In light of equations (32) and (34), and considering the common properties of the Fourier transform with regard to derivatives, we obtain additional key results for the two-dimensional case

$$\begin{aligned} \mathcal{F}\big[\ln R\big] &= -\frac{\pi}{\omega_2} e^{-\omega_2 x_3} \\ \mathcal{F}\left[\frac{{x_2}^2}{R^2}\right] &= -\pi x_3\, e^{-\omega_2 x_3} \\ \mathcal{F}\left[\frac{x_2 x_3}{R^2}\right] &= -i\pi x_3\, e^{-\omega_2 x_3} \\ \mathcal{F}\left[\frac{{x_3}^2}{R^2}\right] &= +\pi x_3\, e^{-\omega_2 x_3} \ , \end{aligned} \tag{35}$$

where the integral transform $\mathcal{F}$ refers to equation (29).

Given the results of equation (35), the Fourier-domain Green's function in anti-plane strain is

$$\hat{g}_{11}(x_3) = \frac{1}{2\mu\omega_2} e^{-\omega_2 x_3} \tag{36}$$

for $x_3 \geq 0$ and $\omega_2 \geq 0$. Considering the symmetry of the displacement with respect to the fault plane, the solution displacement in the Fourier domain for the whole domain is

$$\hat{u}_1(x_3) = \frac{1}{2} \operatorname{sign}(x_3) \hat{s}_1 \, e^{-\omega_2 |x_3|} \tag{37}$$

and the only non-zero traction component is given by

$$\hat{\sigma}_{13} = -\mu \, \omega_2 \frac{\hat{s}_1}{2} e^{-\omega_2 |x_3|} \ , \tag{38}$$

which is compatible with previous inferences (*Idini and Ampuero*, 2020; *Segall*, 2010, Chapter 4.7) for $x_3 = 0$. The displacement and traction for anti-plane strain of equations (37) and (38) can be obtained from the three-dimensional solution of equations (21) and (22), respectively, taking $\hat{s}_2 = 0$, $\omega_1 = 0$, and using $\lim_{\omega_1 \to 0} \omega = |\omega_2|$, providing an alternative derivation.

In-plane strain stress interaction

Finally, and for completeness, let us consider the case of two-dimensional in-plane strain, in which the displacement is in the plane of interest with $u_1 = 0$. Using the plastic strain tensor from equation (1) with $s_1 = 0$, the equivalent body-force simplifies to

$$\mathbf{f} = -\mu \left(s_2 \frac{\partial \delta(x_3)}{\partial x_3} \mathbf{e}_2 + \frac{\partial s_2}{\partial x_2} \delta(x_3) \, \mathbf{e}_3 \right) \ . \tag{39}$$

The solution displacement can be obtained by convolution with the Green's function tensor, as follows

$$u_i(\mathbf{x}) = \iint_{-\infty}^{\infty} g_{ji}(\mathbf{x} - \mathbf{y}) f_j(\mathbf{y}) \, \mathrm{d}\mathbf{y} \ , \tag{40}$$

where the summation is over the indices 2 and 3 and the Green's function components for in-plane strain in a full space are given by

$$\mu \, g_{ij} = \frac{1}{4\pi} \left[\frac{\alpha}{R^2} \left(r_i r_j - \delta_{ij} R^2 \right) - \delta_{ij} (2 - \alpha) \ln R \right] \tag{41}$$

for $i = 2, 3$ and $j = 2, 3$. Combining equations (39) and (40), the displacement field can be expressed as follows

$$\begin{aligned} \frac{1}{\mu} u_2(\mathbf{x}) = & \int_{-\infty}^{\infty} \frac{\partial}{\partial y_3} g_{22}(\mathbf{x} - \mathbf{y}) \big|_{y_3 = 0} s_2 \, \mathrm{d}y_2 \\ & - \int_{-\infty}^{\infty} g_{32}(\mathbf{x} - \mathbf{y}) \big|_{y_3 = 0} \frac{\partial s_2}{\partial y_3} \, \mathrm{d}y_2 \\ \frac{1}{\mu} u_3(\mathbf{x}) = & \int_{-\infty}^{\infty} \frac{\partial}{\partial y_3} g_{23}(\mathbf{x} - \mathbf{y}) \big|_{y_3 = 0} s_2 \, \mathrm{d}y_2 \\ & - \int_{-\infty}^{\infty} g_{33}(\mathbf{x} - \mathbf{y}) \big|_{y_3 = 0} \frac{\partial s_2}{\partial y_2} \, \mathrm{d}y_2 \ . \end{aligned} \tag{42}$$

After Fourier transforming in the x_2 direction based on equation (29), we find

$$
\begin{aligned}
\frac{1}{\mu}\hat{u}_2 &= \frac{\partial}{\partial y_3}\left\{\mathcal{F}[g_{22}]\right\}\hat{s}_2 - \mathcal{F}[g_{32}]\Big|_{y_3=0} i\omega_2\hat{s}_2 \\
\frac{1}{\mu}\hat{u}_3 &= \frac{\partial}{\partial y_3}\left\{\mathcal{F}[g_{23}]\right\}\hat{s}_2 - \mathcal{F}[g_{33}]\Big|_{y_3=0} i\omega_2\hat{s}_2 \; .
\end{aligned}
\tag{43}
$$

The Fourier transform of the Green's function components can be obtained by considering the results of equation (35), giving

$$
\begin{aligned}
\mu\hat{g}_{22} &= \frac{1}{4\omega_2}\left[(2-\alpha)-\alpha\omega_2 x_3\right]e^{-\omega_2 x_3} \\
\mu\hat{g}_{23} = \mu\hat{g}_{32} &= -i\frac{\alpha}{4}x_3\, e^{-\omega_2 x_3} \\
\mu\hat{g}_{33} &= \frac{1}{4\omega_2}\left[(2-\alpha)+\alpha\omega_2 x_3\right]e^{-\omega_2 x_3} \; ,
\end{aligned}
\tag{44}
$$

for $x_3 \geq 0$ and $\omega_2 \geq 0$. Combining equations (43) and (44), and considering the symmetry of displacement about the fault plane and the radiation condition for distant x_3, we obtain the displacement in the full space

$$
\begin{aligned}
\hat{u}_2 &= \frac{\hat{s}_2}{2}\left[\mathrm{sign}(x_3)-\alpha\omega_2 x_3\right]e^{-\omega_2|x_3|} \\
\hat{u}_3 &= -i\frac{\hat{s}_2}{2}\left[(1-\alpha)+\alpha\omega_2|x_3|\right]e^{-\omega_2|x_3|} \; .
\end{aligned}
\tag{45}
$$

The relevant traction components are obtained by application of Hooke's law, to provide

$$
\begin{aligned}
\hat{\sigma}_{23} &= -\mu\alpha\omega_2\hat{s}_2\left(1-\omega_2|x_3|\right)e^{-\omega_2|x_3|} \\
\hat{\sigma}_{33} &= \mu i\alpha\,\omega_2\hat{s}_2\,\omega_2 x_3\, e^{-\omega_2|x_3|} \; .
\end{aligned}
\tag{46}
$$

The displacement and traction components for in-plane strain can be obtained from the three-dimensional solution of equations (21) and (22) with $\hat{s}_1 = 0$, $\omega_1 = 0$, and taking $\lim_{\omega_1\to 0}\omega = |\omega_2|$, thereby demonstrating consistency of the independent derivations.

Applications

The spectral boundary integral method finds a wide range of applications in rupture dynamics to study source processes within seismic cycles. We consider the case of fault slip controlled by a rate- and state-dependent frictional contact. We assume that a quasi-dynamic balance of shear stress and frictional resistance operates at all times. Friction depends on the history of sliding following a physics-based constitutive law that captures the evolution of contact area on the fault plane (*Barbot*, 2019a). The frictional resistance is written as a power-law relationship between stress and slip rate, as follows

$$
V = V_0\left(\frac{\tau}{\mu_0\bar{\sigma}}\right)^{\frac{\mu_0}{a}}\left(\frac{\theta V_0}{L}\right)^{-\frac{b}{a}} \; , \tag{47}
$$

where V is the norm of the sliding velocity vector, V_0 is a reference rate, τ is the norm of the shear traction vector, μ_0 is the reference friction, $\bar{\sigma}$ is the effective normal stress modulated by the pore-fluid pressure, L is the characteristic weakening distance, and the non-dimensional parameters a and b are power exponents. The formulation (47) is preferable to previous formulations due to the underlying physical model (*Barbot*, 2019a) and its validity at vanishing slip-rate. We assume that the state variable follows the aging law in isothermal conditions (*Ruina*, 1983),

$$
\dot{\theta} = 1 - \frac{V\theta}{L} \; . \tag{48}
$$

The quasi-static force balance is described by considering the stress interaction integral equation

$$\dot{t}_i = \int_{\partial\Omega} K_{ji} * (V_j - V_j^L)\,\mathrm{d}A - \frac{\mu}{2V_s}\dot{V}_i \ , \tag{49}$$

where the components of the shear traction are related to the frictional resistance by $\tau^2 = {t_1}^2 + {t_2}^2$ and V_j^L are the j components of the loading rate, possibly heterogeneous. We further assume that the shear traction and sliding velocity vectors are coaligned. The first term on the right-hand side of (49) is a convolution with the stress kernels over the area $\partial\Omega$ of multiple faults and is performed in the Fourier domain, using the transfer function (22) or its two-dimensional equivalents (38) and (46) for anti-plane and in-plane strain, respectively. The stress experienced by any fault is the sum of the self stress and of the one caused by other faults. The second term is the radiation damping corresponding to shear waves radiating away from the fault plane at the speed V_s.

The combination of equations (47-49) forms a closed set describing the evolution of slip and stress. For time stepping, we use four/fifth-order Runge-Kutta explicit time steps (*Press et al.*, 1992). The mean stress-rate is undefined in the Fourier domain without additional constraints, so the driving forces can be specified independently. The mechanical system could be driven by a uniform stress-rate (e.g., *Dublanchet et al.*, 2013), but this would lead to a non-uniform long-term slip accumulation. A specific heterogeneous background stress-rate could also be chosen to produce a uniform long-term slip-rate, but the spatial distribution of stress would be sensitive to the geometry of the fault. Larger faults would slip faster than smaller ones for the same background stress rate. To simplify the model setup, we enforce the long-term loading using a fixed sliding velocity corresponding to the long-term fault slip-rate at the boundary of the domain of integration. In those domains where the velocity is imposed, we do not evaluate the friction law (Figure 1). We conduct simulations for an unbounded space and we do not attempt to approximate a free-surface boundary condition. This simplification is appropriate for the cases considered whereby the seismogenic zone is confined within the middle crust on a vertical fault. We use a discrete Fourier transform to evaluate the stress interactions in the Fourier domain, which introduces a periodicity in the x_1 and x_2 directions, but not in the x_3 direction. We mitigate this issue by padding the computational domain to increase the separation distance between the seismogenic zone with its periodic image. We evaluate the discrete Fourier transforms using the FFTW3 library (*Frigo and Johnson*, 2005) with multi-threaded shared-memory parallelism for the two-dimensional cases that involve one-dimensional Fourier transforms, and with message-passing distributed-memory parallelism for the three-dimensional case that requires two-dimensional Fourier transforms.

The style of ruptures within seismic cycles is controlled by the parameter regime, which can be captured by mostly two non-dimensional parameters describing the properties of the velocity-weakening region (*Barbot*, 2019b). The first is the *Dieterich-Ruina-Rice number*

$$R_u = \frac{W}{h^*} \ , \tag{50}$$

corresponding to a ratio of the seismogenic width W to a characteristic nucleation size h^*, defined as

$$h^* = \frac{\mu L}{(b-a)\bar{\sigma}} \ , \tag{51}$$

where μ is the shear modulus. The actual nucleation size in seismic cycles may vary systematically from the above estimate, but equation (51) is nevertheless useful to define the parameter regime. The second controlling non-dimensional parameter of relevance

$$R_b = \frac{b-a}{b} \ , \tag{52}$$

controls the ratio of static to dynamic stress drops during rupture, affecting the source characteristics.

Seismic cycles for a single velocity-weakening asperity embedded in a velocity-strengthening region will exhibit different styles of rupture and different succession of events depending on the coordinates of the physical parameters in the phase space (R_u, R_b). At intermediate $0.2 < R_b < 1$, the seismic cycle is mainly controlled by the R_u number, with slow-slip events taking place in the range $1 \geq R_u \geq 2$, and slow, periodic bilateral ruptures occurring at higher values $2 \geq R_u \geq 10$, transitioning to cycles of full and partial ruptures for $R_u \geq 20$. For large $R_u \gg 1$ numbers, the seismic cycle becomes increasingly complex, producing ruptures of increasingly varied sizes including foreshock and aftershock sequences (*Barbot*, 2019b; *Cattania*, 2019). For $R_b < 0.1$, the seismic cycle transitions to a regime of slow-slip and slow earthquakes. In particular, slow-slip events become seismogenic for $0 < R_b < 0.1$ and $R_u \gg 1$ (*Barbot*, 2019b).

Exploration of fault dynamics for large R_u numbers, whether for small or intermediate R_b values, is challenging because numerical models must resolve the smallest value taken by the cohesion length (*Dieterich*, 1992, 1994; *Rubin and Ampuero*, 2005)

$$L_b = \frac{GL}{b\bar{\sigma}} \ , \tag{53}$$

which is often many times smaller than the nucleation size in velocity-weakening domains. Parameter regimes leading to vanishing $R_b > 0$ at high R_u number are particularly demanding numerically because they correspond to vanishingly small cohesion size. In the next sub-section, we will illustrate models of seismic cycles corresponding to these parameter regimes for a single fault using a two-dimensional setting.

Sequences of partial and full ruptures

In this section, we describe the evolution of fault slip on two-dimensional faults within the anti-plane strain approximation. We first consider the case of a long strike-slip fault with a single velocity-weakening asperity with a comparatively much smaller characteristic nucleation size. Specifically, we consider the combination of physical properties $\mu_0 = 0.6$, $a = 10^{-2}$, $b = 1.4 \times 10^{-2}$, $L = 250\,\mu\text{m}$, $\bar{\sigma} = 100\,\text{MPa}$ in the velocity-weakening region leading to $R_u = 266$ and $R_b = 0.285$. In the velocity-strengthening region, we have $b = 6 \times 10^{-3}$. The cohesion size is $L_b = 5.35\,\text{m}$ and the width of the velocity-weakening asperity is $W = 5\,\text{km}$. We discretize the fault with 2^{15} elements with a sampling size of $0.5\,\text{m}$ and simulate the fault slip evolution for a period of 300 years encompassing 220 seismic ruptures, representing 8,000,000 time steps. We dedicate 100 samples at both ends of the domain to enforce a long-term slip-rate of 1 nm/s. This loading rate, equivalent to 31.5 mm/yr, is representative of geological slip rates on major continental strike-slip faults. The simulation takes 46 hours running on 8 parallel cores.

The seismic cycle exhibits much complexity, with rupture size varying within fractions of the velocity-weakening asperity width (Figure 2a). All ruptures initiate close to the transition from velocity-weakening to velocity-strengthening. Most ruptures feature a sharp pulse-like front with occasional back-propagating fronts that cause multi-pulse ruptures. Tiny events occur during the postseismic period of large earthquakes while afterslip spreads in the velocity-strengthening region. Ruptures initiate on both sides of the seismogenic zone, but the cycle includes full and partial ruptures succeeding in an aperiodic sequence. The partial ruptures most often reside within a half of the seismogenic zone, starting on either side. The distribution of rupture sizes, expressed in moment per unit length because of the two-dimensional setting, approaches a power law (Figure 2c).

These results highlight the complexity that emerges for certain parameter regimes, here, for $R_u \gg 1$. While the spectral boundary integral method dramatically improves the numerical efficiency compared to the space-domain method, exploring the behavior of faults with even higher R_u numbers will still constitute a major challenge.

Seismogenic slow-slip events

We now explore another end-member frictional parameter regime corresponding to seismogenic slow-slip events. While it is widely recognized that aseismic slow-slip events occur spontaneously within velocity-weakening asperities with dimensions commensurate with the nucleation size (e.g. *Liu and Rice*, 2005, and references therein), seismogenic slow-slip events develop in a broad range of parameters leading to vanishing $R_b > 0$ and $R_u \gg 1$ (*Barbot*, 2019b). However, simulations of seismic cycles in this parameter range are particular challenging because resolving the small cohesion size while capturing the overall domain size requires exceedingly many degrees of freedom. We present numerical simulations of seismogenic slow-slip events in this numerically demanding parameter regime.

We consider a single homogeneous velocity-weakening asperity embedded in a velocity-strengthening fault. The physical properties $\mu_0 = 0.6$, $a = 8 \times 10^{-2}$, $b = 8.163 \times 10^{-2}$, $L = 70\,\mu\text{m}$, $\bar{\sigma} = 20\,\text{MPa}$ in the velocity-weakening region lead to $R_u = 77$ and $R_b = 0.02$. The cohesive size is $L_b = 1.29\,\text{m}$ and the width of the velocity-weakening domain is $W = 5\,\text{km}$. We discretize the domain with 2^{16} elements using a sampling size of 0.2 m, resolving the cohesive zone by a factor of 6.4. We load the system at a rate of 1 nm/s in the far-field for a period of 20 years. The simulation requires 3,000,000 time steps and takes 35 hours using 4 shared-memory cores.

The simulation produces an aperiodic sequence of 8 slow-slip events characterized by up-dip and down-dip migrating rupture fronts that cause localized seismogenic ruptures when they meet and coalesce (Figure 2). The sequence includes 22 events with peak velocity above 0.1 m/s, firmly in the seismogenic range. However, the background ruptures last between 0.4 and 0.9 years with recurrence times between 1.3 and 3 years, clearly the hallmark of slow slip. Because of the complex interactions between slow and fast slip, the sequence is chaotic, with the details of successive slow-slip events ever changing. Each slow-slip event starts with a pair of rupture fronts converging inward, provoking a seismic event when they coalesce. The collision of the rupture fronts sparks diverging rupture fronts that subsequently trigger back-propagating creep fronts. The coalescence of these rupture fronts occasionally triggers other seismic ruptures that allow the cascade of anastomosing creep waves to continue for weeks, until the background slow slip reaches the boundary of the tremorgenic zone.

These results confirm the need for numerically efficient numerical methods to explore important regions of the parameter space that will otherwise remain overlooked. The quasi-dynamic spectral integral method will be key to explore the dynamics of seismogenic slow-slip events because of its numerical efficiency and the predominance of aseismic slip.

Restraining step-over

In this section, we illustrate the capability of the spectral boundary integral method to include several parallel faults. We use the in-plane strain approximation to simulate fault dynamics across a restraining step-over consisting of the two left-lateral strike-slip faults separated by an offset with overlap (Figure 3b). Contractional steps represents an idealization of restraining bends and push-up structures commonly found at segment boundaries across continental transforms that have been modeled extensively (*Harris et al.*, 1991; *Harris and Day*, 1993; *Lozos et al.*, 2011; *Oglesby*, 2005, 2008; *Duan and Oglesby*, 2006; *Bai and Ampuero*, 2017; *Romanet et al.*, 2018). The faults overlap horizontally by 5 km and are separated by a perpendicular distance of 2.5 km, as commonly observed (*Wesnousky*, 2006). The velocity-weakening regions are 6.5 km long and their horizontal overlap is 3 km. We consider different properties for each fault, so that they would develop distinct seismic cycles if operating in isolation. Common parameters include $a = 10^{-2}$, $L = 5\,\text{mm}$, a rigidity of 30 GPa, $\mu_0 = 0.6$ and $b = 6 \times 10^{-3}$ in the velocity-strengthening region. For fault A, we use $\bar{\sigma} = 100\,\text{MPa}$, leading to $R_u = 17.33$ and $R_b = 0.285$. For fault B, we use $\bar{\sigma} = 125\,\text{MPa}$, leading to $R_u = 21.66$ and $R_b = 0.285$. We use different normal stress, which controls the recurrence time of earthquakes, to avoid automatic synchronization of the ruptures on both sides. Each fault is discretized with 2048 elements of 10 m length. We construct the step-over by pinning the regions beyond the overlap, as they must be included in the stress calculation for the Fourier-domain solution to work properly. The pinned regions are included in the stress interaction calculation, but not in the evaluation of the constitutive law. Simulating over 300 years of fault slip evolution with 200,000 time steps take 30 minutes with a dual core computer.

When considered in isolation, the seismic cycle on these faults is quite different, as they operate under different parameter regimes in the (R_u, R_b) space. Fault A converges to a limit cycle with a period-four sequence of full ruptures of the seismogenic zone alternating with either a slow-slip event or a seismic partial rupture (Figure 3a). Fault B falls into a period-two sequence of full ruptures alternating with a partial rupture with consistent nucleation sites (Figure 3c). When the mechanical interactions between the two faults are taken into account, they both follow an aperiodic sequence of full and partial ruptures punctuated by occasional slow-slip events (Figure 3b). We find that no rupture jumps across the step-over, compatible with previous findings for a contractional step-over with such separation distance (*Oglesby*, 2008; *Bai and Ampuero*, 2017), but the perturbation of the seismic sequence within the step-over in terms of rupture styles and recurrence patterns is considerable.

While further studies of fault dynamics at step-overs within seismic cycles are warranted to explore a wide parameter space, the current results illustrate the potential of the spectral boundary integral method to resolve long sequence of fault evolution on two-dimensional fault systems with geometrical complexity with a reasonable computational burden.

Parallel strike-slip faults of finite dimension

Finally, we illustrate the capability of incorporating multiple parallel faults in three-dimensional models of fault dynamics with the spectral boundary integral method. We consider the case of multiple parallel strike-slip faults, as is found at the termination of continental strike-slip faults in California, Anatolia, and New Zealand. We consider a case inspired by the structural layout of the Southern California section of the San Andreas Fault where the relative motion between the Pacific and North American plates is partitioned among the Inglewood-Newport-Rose Canyon, Elsinore, San Jacinto, and San Andreas faults (e.g., *Barbot*, 2020b).

For simplicity, we consider fault segments with identical physical properties. The four faults are 102.4 km long, each discretized with 2^{10} elements along strike and 2^8 elements with depth, with a sampling size of 200 m (Figure 4). The seismogenic zone extends 75 km along-strike and 10 km down-dip. We use 40 elements around the rectangle domain to impose an identical loading on all faults as a boundary condition. When considering a single fault in isolation, we use a loading rate of 1 nm/s (i.e., 31.5 mm/yr). When the four faults accommodate slip partitioning, we use a loading of 0.25 nm/s on all faults, such that the long-term cumulative deformation is equivalent across one or four faults. The fault separation distances are 41, 37, and 36 km, commensurate with the Southern California system.

We first compare the responses of the single-fault and partitioned systems using identical frictional properties. We use the common parameters $\mu_0 = 0.6$, $a = 10^{-2}$, $b = 1.4 \times 10^{-2}$, $\bar{\sigma} = 100\,\text{MPa}$, and $L = 25\,\text{mm}$, and a uniform elastic Poisson's solid with a rigidity of 30 GPa. This leads to $R_u = 5.33$ and $R_b = 0.285$. We sample the cohesive zone by a factor of 5.4 using a sampling size of 100 m. We simulate fault dynamics for a period of 300 years. The calculation represents close to 700,000 time steps, which takes 10 hours for a single fault and 55 hours with four faults, using 16 cores in both cases.

The seismic cycle on a single, isolated fault with these properties already exhibits some complexity, due to the two characteristics length scales present in the system associated with the large aspect ratio of the velocity-weakening region (Figure 4a). When the fault is decoupled from its neighbors, the seismic cycle initiates with a series of through-going ruptures of moment magnitude 7.0. This is soon followed by more complex sequences of partial ruptures that break the sides and central sections of the seismogenic zone, followed by slow-slip episodes representing failed nucleations. The cycle of full ruptures and rapid sequences of partial ruptures are relatively constant with recurrence times of about 80 years (Figure 4e). However, many seismic clusters occur, corresponding to rapid successive failures of small portions of the seismogenic zone corresponding to moment magnitude 6.5 earthquakes. The complexity of seismic cycles on elongated faults is well recognized (e.g., *Hirose and Hirahara*, 2002, 2004; *Weng and Ampuero*, 2019), but elastic coupling between parallel faults adds further features (Figure 4b,d). With quasi-static stress transfer among faults, the sequence includes long hiatus (up to 185 years), short aseismic periods (down to just 10 years) between subsequent ruptures on some faults, and overall more complexity in recurrence patterns.

We then illustrate the impact of frictional properties on the degree of interactions of parallel faults. We consider identical frictional properties on all faults, but we simulate cases with $L = 25$, 18.5, and 12.5 mm, corresponding to R_u numbers of 5, 7, and 10, respectively. The simulations for the smallest characteristic weakening distance are more challenging and take 75 hours for four faults. For $R_u = 5$, the interaction among faults is week, with only a few large earthquakes occurring shortly after another on a neighboring fault (Figure 5a). For $R_u = 7$, all large earthquakes are clustered, following each other only by a few years (Figure 5b). For $R_u = 10$, the mechanical interactions are much stronger, leading to synchronization of ruptures between neighboring faults (Figure 5c). Increasing R_u numbers correspond to reducing characteristic nucleation size, making the faults more unstable, and more susceptible to triggering. These simulations show the strong control of frictional properties on the recurrence pattern of large earthquakes on parallel faults, with increasing R_u leading to stronger fault interactions within the network, towards tight synchronization of seismicity.

These results illustrate the potential of the spectral boundary integral method to simulate quasi-static stress transfers among parallel finite faults with high enough numerical efficiency to capture the geometry of large fault systems at tectonic plate boundaries.

Conclusions

The study derives the quasi-dynamic spectral boundary integral method for multiple parallel faults for finite faults and in two-dimensional approximations. The method is effective to simulate single faults with many degrees of freedom, which is relevant for challenging parameter regimes, or to model networks of faults. The method expands the range of applicability of the spectral boundary integral method to a network of multiple parallel faults while maintaining the numerical efficiency associated with the fast Fourier transform. The approach should be useful for many problems of geophysical interest involving geometrical complexity or mechanical interactions within a fault network, as is found at many continental tectonic plate boundaries.

Data and Resources

The author confirms that the data supporting the findings of this study are available within the article. The supplemental material includes Figure S1, showing displacement and stress calculated in the Fourier domain, and Figure S2, showing the difference between the Fourier-domain and space-domain stress calculations.

Acknowledgments

This study was supported in part by the National Science Foundation under award number EAR-1848192.

Conflict of interest

The authors declare no conflict of interest.

References

Aagaard, B. T., T. H. Heaton, and J. F. Hall, Dynamic earthquake ruptures in the presence of lithostatic normal stresses: Implications for friction models and heat production, *Bull. Seism. Soc. Am.*, *91*(6), 1765–1796, doi:10.1785/0120000257, 2001.

Aagaard, B. T., M. G. Knepley, and C. A. Williams, A domain decomposition approach to implementing fault slip in finite-element models of quasi-static and dynamic crustal deformation, *J. Geophys. Res.*, *118*(6), 3059–3079, 2013.

Aki, K., and P. G. Richards, *Quantitative Seismology*, vol. I, W. H. Freeman and company, New York, 1980.

Ando, R., Fast Domain Partitioning Method for dynamic boundary integral equations applicable to non-planar faults dipping in 3-D elastic half-space, *Geophys. J. Int.*, *207*(2), 833–847, doi:10.1093/gji/ggw299, 2016.

Ando, R., and Y. Kaneko, Dynamic rupture simulation reproduces spontaneous multifault rupture and arrest during the 2016 Mw 7.9 Kaikoura earthquake, *Geophys. Res. Lett.*, *45*(23), 12–875, doi:10.1029/2018GL080550, 2018.

Andrews, D., Dynamic plane-strain shear rupture with a slip-weakening friction law calculated by a boundary integral method, *Bull. Seism. Soc. Am.*, *75*(1), 1–21, 1985.

Andrews, D. J., Rupture propagation with finite stress in antiplane strain, *J. Geophys. Res.*, *81*, 3575–3582, doi:10.1029/JB081i020p03575, 1976.

Aochi, H., and E. Fukuyama, Three-dimensional nonplanar simulation of the 1992 Landers earthquake, *J. Geophys. Res.*, *107*(B2), ESE–4, doi:10.1029/2000JB000061, 2002.

Bai, K., and J.-P. Ampuero, Effect of seismogenic depth and background stress on physical limits of earthquake rupture across fault step overs, *J. Geophys. Res.*, *122*(12), 10–280, 2017.

Barbot, S., Deformation of a half-space from anelastic strain confined in a tetrahedral volume, *Bull. Seism. Soc. Am.*, *108*(5A), 2687, doi:10.1785/0120180058, 2018a.

Barbot, S., Asthenosphere flow modulated by megathrust earthquake cycles, *Geophys. Res. Lett.*, *45*, 6018–6031, doi:10.1029/2018GL078197, 2018b.

Barbot, S., Modulation of fault strength during the seismic cycle by grain-size evolution around contact junctions, *Tectonophysics*, *765*, 129–145, doi:10.1016/j.tecto.2019.05.004, 2019a.

Barbot, S., Slow-slip, slow earthquakes, period-two cycles, full and partial ruptures, and deterministic chaos in a single asperity fault, *Tectonophysics*, *768*, 228,171, doi:10.1016/j.tecto.2019.228171, 2019b.

Barbot, S., Frictional and structural controls of seismic super-cycles at the Japan trench, *Earth Planets Space*, *72*(63), doi:10.1186/s40623-020-01185-3, 2020a.

Barbot, S., Mantle flow distribution beneath the California margin, *Nature Communications*, *11*(1), 1–14, doi:10.1038/s41467-020-18260-8, 2020b.

Barbot, S., and Y. Fialko, Fourier-domain Green's function for an elastic semi-infinite solid under gravity, with applications to earthquake and volcano deformation, *Geophys. J. Int.*, *182*(2), 568–582, doi:10.1111/j.1365-246X.2010.04655.x, 2010.

Barbot, S., Y. Fialko, and D. Sandwell, Three-Dimensional Models of Elasto-Static Deformation in Heterogeneous Media, with Applications to the Eastern California Shear Zone, *Geophys. J. Int.*, *179*(1), 500–520, doi:10.1111/j.1365-246X.2009.04194.x, 2009.

Barbot, S., N. Lapusta, and J. P. Avouac, Under the hood of the earthquake machine: Towards predictive modeling of the seismic cycle, *Science*, *336*(6082), 707–710, doi:10.1126/science.1218796, 2012.

Barbot, S., J. D. Moore, and V. Lambert, Displacement and stress associated with distributed anelastic deformation in a half-space, *Bull. Seism. Soc. Am.*, *107*(2), 821–855, doi:10.1785/0120160237, 2017.

Bhat, H. S., M. Olives, R. Dmowska, and J. R. Rice, Role of fault branches in earthquake rupture dynamics, *J. Geophys. Res.*, *112*(B11309), 16, doi:10.1029/2007JB005027, 2007.

Bouchon, M., and F. J. Sánchez-Sesma, Boundary integral equations and boundary elements methods in elastodynamics, *Advances in geophysics*, *48*, 157–189, doi:10.1016/S0065-2687(06)48003-1, 2007.

Bouchon, M., and D. Streiff, Propagation of a shear crack on a nonplanar fault: A method of calculation, *Bull. Seism. Soc. Am.*, *87*(1), 61–66, 1997.

Bouchon, M., M. Campillo, and S. Gaffet, A boundary integral equation-discrete wavenumber representation method to study wave propagation in multilayered media having irregular interfaces, *Geophysics*, *54*(9), 1134–1140, doi:10.1190/1.1442748, 1989.

Bradley, A. M., Software for efficient static dislocation–traction calculations in fault simulators, *Seism. Res. Lett.*, *85*(6), 1358–1365, doi:10.1785/0220140092, 2014.

Cattania, C., Complex earthquake sequences on simple faults, *Geophys. Res. Lett.*, *46*(17-18), 10,384–10,393, doi:10.1029/2019GL083628, 2019.

Chen, T., and N. Lapusta, Scaling of small repeating earthquakes explained by interaction of seismic and aseismic slip in a rate and state fault model, *J. Geophys. Res.*, *114*(B01311), 12 PP., 2009.

Chen, X., and H. Zhang, Modelling rupture dynamics of a planar fault in 3-d half space by boundary integral equation method: An overview, *Pure Appl. Geophys.*, *163*(2-3), 267–299, doi:10.1007/s00024-005-0020-z, 2006.

Dal Zilio, L., N. Lapusta, and J.-P. Avouac, Unraveling scaling properties of slow-slip events, *Geophys. Res. Lett.*, *47*(10), e2020GL087,477, doi:10.1029/2020GL087477, 2020.

Day, S. M., Three-dimensional finite difference simulation of fault dynamics: rectangular faults with fixed rupture velocity, *Bull. Seism. Soc. Am.*, *72*(3), 705–727, 1982.

Dieterich, J., A constitutive law for rate of earthquake production and its application to earthquake clustering, *J. Geophys. Res.*, *99*(B2), 2601–2618, doi:10.1029/93JB02581, 1994.

Dieterich, J. H., Earthquake nucleation on faults with rate- and state-dependent strength, *Tectonophysics*, *211*, 115–134, doi:10.1016/0040-1951(92)90055-B, 1992.

Dinther, Y. v., T. V. Gerya, L. A. Dalguer, P. M. Mai, G. Morra, and D. Giardini, The seismic cycle at subduction thrusts: Insights from seismo-thermo-mechanical models, *J. Geophys. Res.*, *118*(12), 6183–6202, doi:10.1002/2013JB010380, 2013.

Duan, B., Role of initial stress rotations in rupture dynamics and ground motion: A case study with implications for the Wenchuan earthquake, *J. Geophys. Res.*, *115*(B5), doi:10.1029/2009JB006750, 2010.

Duan, B., and D. D. Oglesby, Multicycle dynamics of nonplanar strike-slip faults, *J. Geophys. Res.*, *110*(B3), 2005.

Duan, B., and D. D. Oglesby, Heterogeneous fault stresses from previous earthquakes and the effect on dynamics of parallel strike-slip faults, *J. Geophys. Res.*, *111*(B5), doi:10.1029/2005JB004138, 2006.

Dublanchet, P., Inferring fault slip rates from cumulative seismic moment in a multiple asperity context, *Geophys. J. Int.*, *216*(1), 395–413, doi:10.1093/gji/ggy431, 2019.

Dublanchet, P., Stress-dependent b value variations in a heterogeneous rate-and-state fault model, *Geophys. Res. Lett.*, *47*(13), e2020GL087,434, doi:10.1029/2020GL087434, 2020.

Dublanchet, P., P. Bernard, and P. Favreau, Interactions and triggering in a 3-d rate-and-state asperity model, *J. Geophys. Res.*, *118*(5), 2225–2245, doi:10.1002/jgrb.50187, 2013.

Frigo, M., and S. G. Johnson, The design and implementation of FFTW3, *Proceedings of the IEEE*, *93*(2), 216–231, 2005.

Fukahata, Y., and M. Matsu'ura, General expressions for internal deformation fields due to a dislocation source in a multilayered elastic half-space, *Geophys. J. Int.*, *161*(2), 507–521, doi:10.1111/j.1365-246X.2005.02594.x, 2005.

Fukuyama, E., and R. Madariaga, Dynamic propagation and interaction of a rupture front on a planar fault, in *Microscopic and Macroscopic Simulation: Towards Predictive Modelling of the Earthquake Process*, pp. 1959–1979, Springer, doi:10.1007/978-3-0348-7695-7_9, 2000.

Gabriel, A.-A., J.-P. Ampuero, L. A. Dalguer, and P. M. Mai, The transition of dynamic rupture styles in elastic media under velocity-weakening friction, *J. Geophys. Res.*, *117*(B9), 2012.

Gallovič, F., Heterogeneous coulomb stress perturbation during earthquake cycles in a 3d rate-and-state fault model, *Geophys. Res. Lett.*, *35*(21), doi:10.1029/2008GL035614, 2008.

Geubelle, P. H., and J. R. Rice, A spectral method for three-dimensional elastodynamic fracture problems, *J. Mech. Phys. Solids*, *43*, 1791–1824, 1995.

Gilbert, F., and G. Backus, Propagator matrices in elastic wave and vibration problems, *Geophysics*, *31*(2), 326–332, doi:10.1190/1.1439771, 1966.

Harris, R. A., and S. M. Day, Dynamics of fault interaction: Parallel strike-slip faults, *J. Geophys. Res.*, *98*(B3), 4461–4472, doi:10.1029/92JB02272, 1993.

Harris, R. A., R. J. Archuleta, and S. M. Day, Fault steps and the dynamic rupture process: 2-d numerical simulations of a spontaneously propagating shear fracture, *Geophys. Res. Lett.*, *18*(5), 893–896, doi:10.1029/91GL01061, 1991.

Hirose, H., and K. Hirahara, A model for complex slip behavior on a large asperity at subduction zones, *Geophys. Res. Lett.*, *29*(22), 25–1, doi:10.1007/s00024-002-8731-x, 2002.

Hirose, H., and K. Hirahara, A 3-d quasi-static model for a variety of slip behaviors on a subduction fault, *Pure Appl. Geophys.*, *161*(11-12), 2417–2431, doi:10.1007/s00024-004-2573-7, 2004.

Hori, T., and S. Miyazaki, A possible mechanism of M 9 earthquake generation cycles in the area of repeating M 7∼8 earthquakes surrounded by aseismic sliding, *Earth Planets Space*, *63*(7), 48, 2011.

Idini, B., and J.-P. Ampuero, Fault-zone damage promotes pulse-like rupture and back-propagating fronts via quasi-static effects, *Geophys. Res. Lett.*, *47*(23), e2020GL090,736, doi:10.1029/2020GL090736, 2020.

Jiang, J., and N. Lapusta, Deeper penetration of large earthquakes on seismically quiescent faults, *Science*, *352*(6291), 1293–1297, 2016.

Kaneko, Y., N. Lapusta, and J.-P. Ampuero, Spectral element modeling of spontaneous earthquake rupture on rate and state faults: Effect of velocity-strengthening friction at shallow depths, *J. Geophys. Res.*, *113*, 17, 2008.

Kase, Y., and S. Day, Spontaneous rupture processes on a bending fault, *Geophys. Res. Lett.*, *33*(10), doi:10.1029/2006GL025870, 2006.

Kato, N., Seismic cycle on a strike-slip fault with rate-and state-dependent strength in an elastic layer overlying a viscoelastic half-space, *Earth Planets Space*, *54*(11), 1077–1083, doi:10.1186/BF03353305, 2002.

Lambert, V., and S. Barbot, Contribution of viscoelastic flow in earthquake cycles within the lithosphere-asthenosphere system, *Geophys. Res. Lett.*, *43*(19), 142–154, doi:10.1002/2016GL070345, 2016.

Lapusta, N., and S. Barbot, Models of earthquakes and aseismic slip based on laboratory-derived rate and state friction laws, in *The mechanics of Faulting: From Laboratory to Real Earthquakes*, edited by A. Bizzarri and H. S. Bhat, pp. 153–207, Research Signpost, Trivandrum, Kerala, India, 2012.

Lapusta, N., and Y. Liu, Three-dimensional boundary integral modeling of spontaneous earthquake sequences and aseismic slip, *J. Geophys. Res.*, *114*(B09303), 25 PP., 2009.

Lapusta, N., and J. R. Rice, Nucleation and early seismic propagation of small and large events in a crustal earthquake model, *J. Geophys. Res.*, *108*(B4, 2205), doi:10.1029/2001JB000793, 2003.

Lapusta, N., J. R. Rice, Y. BenZion, and G. Zheng, Elastodynamics analysis for slow tectonic loading with spontaneous rupture episodes on faults with rate- and state-dependent friction, *J. Geophys. Res.*, *105*(B10), 23,765–23,789, 2000.

Leeman, J., D. Saffer, M. Scuderi, and C. Marone, Laboratory observations of slow earthquakes and the spectrum of tectonic fault slip modes, *Nature Communications*, *7*, 11,104, doi:10.1038/ncomms11104, 2016.

Li, D., and Y. Liu, Spatiotemporal evolution of slow slip events in a nonplanar fault model for northern cascadia subduction zone, *J. Geophys. Res.*, *121*(9), 6828–6845, 2016.

Li, D., and Y. Liu, Modeling slow-slip segmentation in cascadia subduction zone constrained by tremor locations and gravity anomalies, *J. Geophys. Res.*, *122*(4), 3138–3157, 2017.

Liu, Y., and J. R. Rice, Aseismic slip transients emerge spontaneously in three-dimensional rate and state modeling of subduction earthquake sequences, *J. Geophys. Res.*, *110*(B08307), doi:10.1029/2004JB003424, 2005.

Liu, Y. J., J. J. McGuire, and M. D. Behn, Frictional behavior of oceanic transform faults and its influence on earthquake characteristics, *J. Geophys. Res.*, *117*(B04315), 10.1029/2011JB009,025, 2012.

Lozos, J. C., D. D. Oglesby, B. Duan, and S. G. Wesnousky, The effects of double fault bends on rupture propagation: A geometrical parameter study, *Bull. Seism. Soc. Am.*, *101*(1), 385–398, doi:10.1785/0120100029, 2011.

Luo, B., B. Duan, and D. Liu, 3D Finite-Element Modeling of Dynamic Rupture and Aseismic Slip over Earthquake Cycles on Geometrically Complex Faults, *Bull. Seism. Soc. Am.*, *110*(6), 2619–2637, doi:10.1785/0120200047, 2020.

Ma, X., S. Hajarolasvadi, G. Albertini, D. S. Kammer, and A. E. Elbanna, A hybrid finite element-spectral boundary integral approach: Applications to dynamic rupture modeling in unbounded domains, *International Journal for Numerical and Analytical Methods in Geomechanics*, *43*(1), 317–338, doi:10.1002/nag.2865, 2019.

Madariaga, R., Dynamics of an expanding circular fault, *Bull. Seism. Soc. Am.*, *66*(3), 639–666, 1976.

Matsuzawa, T., H. Hirose, B. Shibazaki, and K. Obara, Modeling short- and long-term slow slip events in the seismic cycles of large subduction earthquakes, *J. Geophys. Res.*, *115*(B12301), doi:10.1029/2010JB007566, 2010.

Noda, H., and N. Lapusta, Three-dimensional earthquake sequence simulations with evolving temperature and pore pressure due to shear heating: Effect of heterogeneous hydraulic diffusivity, *J. Geophys. Res.*, *115*(B12314), 24 PP., doi:10.1029/2010JB007780, 2010.

Noda, H., D. S. Sato, and Y. Kurihara, Comparison of two time-marching schemes for dynamic rupture simulation with a space-domain BIEM, *Earth Planets Space*, *72*(1), 1–12, doi:10.1186/s40623-020-01202-5, 2020.

Obara, K., and A. Kato, Connecting slow earthquakes to huge earthquakes, *Science*, *353*(6296), 253–257, doi:10.1126/science.aaf1512, 2016.

Oglesby, D., Rupture termination and jump on parallel offset faults, *Bull. Seism. Soc. Am.*, *98*(1), 440–447, doi:10.1785/0120070163, 2008.

Oglesby, D. D., The dynamics of strike-slip step-overs with linking dip-slip faults, *Bull. Seism. Soc. Am.*, *95*(5), 1604–1622, doi:10.1785/0120050058, 2005.

Oglesby, D. D., and R. J. Archuleta, The three-dimensional dynamics of a nonplanar thrust fault, *Bull. Seism. Soc. Am.*, *93*(5), 2222–2235, doi:10.1785/0120020204, 2003.

Oglesby, D. D., and S. M. Day, Stochastic fault stress: Implications for fault dynamics and ground motion, *Bull. Seism. Soc. Am.*, *92*(8), 3006–3021, doi:10.1785/0120010249, 2002.

Ohtani, M., K. Hirahara, T. Hori, and M. Hyodo, Observed change in plate coupling close to the rupture initiation area before the occurrence of the 2011 tohoku earthquake: Implications from an earthquake cycle model, *Geophys. Res. Lett.*, *41*(6), 1899–1906, 2014.

Okada, Y., Internal deformation due to shear and tensile faults in a half-space, *Bull. Seism. Soc. Am.*, *82*, 1018–1040, 1992.

Ong, M., Su Qing, S. Barbot, and J. Hubbard, Physics-based scenario of earthquake cycles on the Ventura Thrust system, California: the effect of variable friction and fault geometry, *Pure Appl. Geophys.*, doi:10.1007/s00024-019-02111-9, 2019.

Otani, Y., T. Takahashi, and N. Nishimura, A fast boundary integral equation method for elastodynamics in time domain and its parallelisation, in *Boundary Element Analysis*, pp. 161–185, Springer, doi:10.1007/978-3-540-47533-0_7, 2007.

Pan, E., Green's functions for geophysics: A review, *Reports on Progress in Physics*, *82*(10), 106,801, doi:101088/1361-6633/ab1877, 2019.

Pelties, C., J. De la Puente, J.-P. Ampuero, G. B. Brietzke, and M. Käser, Three-dimensional dynamic rupture simulation with a high-order discontinuous Galerkin method on unstructured tetrahedral meshes, *J. Geophys. Res.*, *117*(B2), doi:10.1029/2011JB008857, 2012.

Perrin, G., J. R. Rice, and G. Zheng, Self-healing slip pulse on a frictional surface, *J. Mech. Phys. Sol.*, *43*, 1461–1495, 1995.

Press, W. H., S. A. Teukolsky, W. T. Vetterling, and B. P. Flannery, *Numerical Recipes in C: The Art of Scientific Computing*, 2nd ed., 994 pp., Cambridge Univ. Press, New York, 1992.

Puente, J., J.-P. Ampuero, and M. Käser, Dynamic rupture modeling on unstructured meshes using a discontinuous galerkin method, *J. Geophys. Res.*, *114*(B10), 2009.

Rezakhani, R., F. Barras, M. Brun, and J.-F. Molinari, Finite element modeling of dynamic frictional rupture with rate and state friction, *J. Mech. Phys. Solids*, p. 103967, doi:10.1016/j.jmps.2020.103967, 2020.

Rice, J. R., Spatio-temporal complexity of slip on a fault, *J. Geophys. Res.*, *98*(B6), 9885–9907, doi:10.1029/93JB00191, 1993.

Romanet, P., H. S. Bhat, R. Jolivet, and R. Madariaga, Fast and slow slip events emerge due to fault geometrical complexity, *Geophys. Res. Lett.*, *45*, 4809–4819, 2018.

Rubin, A. M., and J.-P. Ampuero, Earthquake nucleation on (aging) rate and state faults, *J. Geophys. Res.*, *110*(B11312), 24 PP., doi:10.1029/2005JB003686, 2005.

Ruina, A., Slip instability and state variable friction laws, *J. Geophys. Res.*, *88*, 10,359–10,370, doi:10.1029/JB088iB12p10359, 1983.

Sathiakumar, S., S. Barbot, and J. Hubbard, Seismic cycles in fault-bend folds, *J. Geophys. Res.*, *125*(8), e2019JB018,557, doi:10.1029/2019JB018557, 2020.

Sato, R., and M. Matsu'ura, Static deformations due to the fault spreading over several layers in a multi-layered medium, *J. Phys. Earth*, *21*(3), 227–249, 1973.

Segall, P., *Earthquake and volcano deformation*, Princeton University Press, Princeton, NJ, 2010.

Shi, Q., S. Barbot, B. Shibazaki, T. Matsuzawa, S. Wei, and P. Tapponnier, Structural control and system-level behavior of the seismic cycle at the Nankai trough, *Earth Planets Space*, *72*(1), 1–31, doi:10.1186/s40623-020-1145-0, 2020.

Smith, B., and D. Sandwell, A three-dimensional semianalytic viscoelastic model for time-dependent analyses of the earthquake cycle, *J. Geophys. Res.*, *109*, 2004.

Steketee, J. A., On Volterra's Dislocations in a Semi-Infinite Elastic Medium, *Can. J. Phys.*, *36*, 192–205, 1958.

Tada, T., Boundary integral equation method for earthquake rupture dynamics, *International Geophysics*, *94*, 217–267, doi:10.1016/S0074-6142(08)00009-0, 2009.

Tago, J., V. M. Cruz-Atienza, J. Virieux, V. Etienne, and F. J. Sánchez-Sesma, A 3d hp-adaptive discontinuous galerkin method for modeling earthquake dynamics, *J. Geophys. Res.*, *117*(B9), doi:10.1029/2012JB009313, 2012.

Thakur, P., Y. Huang, and Y. Kaneko, Effects of low-velocity fault damage zones on long-term earthquake behaviors on mature strike-slip faults, *J. Geophys. Res.*, *125*(8), e2020JB019,587, doi:10.1029/2020JB019587, 2020.

Thomas, M. Y., N. Lapusta, H. Noda, and J.-P. Avouac, Quasi-dynamic versus fully dynamic simulations of earthquakes and aseismic slip with and without enhanced coseismic weakening, *J. Geophys. Res.*, *119*(3), 1986–2004, doi:10.1002/2013JB010615, 2014.

Tse, S. T., and J. R. Rice, Crustal earthquake instability in relation to the depth variation of frictional slip properties, *J. Geophys. Res.*, *91*(B9), 9452–9472, 1986.

Ulrich, T., A.-A. Gabriel, J.-P. Ampuero, and W. Xu, Dynamic viability of the 2016 mw 7.8 kaikōura earthquake cascade on weak crustal faults, *Nature Communications*, *10*(1), 1213, 2019.

Uphoff, C., S. Rettenberger, M. Bader, E. H. Madden, T. Ulrich, S. Wollherr, and A.-A. Gabriel, Extreme scale multi-physics simulations of the tsunamigenic 2004 sumatra megathrust earthquake, in *Proceedings of the International Conference for High Performance Computing, Networking, Storage and Analysis*, p. 21, ACM, 2017.

Van Zelst, I., S. Wollherr, A.-A. Gabriel, E. H. Madden, and Y. van Dinther, Modeling megathrust earthquakes across scales: One-way coupling from geodynamics and seismic cycles to dynamic rupture, *J. Geophys. Res.*, *124*(11), 11,414–11,446, doi:10.1029/2019JB017539, 2019.

Veedu, D., and S. Barbot, The Parkfield tremors reveal slow and fast ruptures on the same asperity, *Nature*, *532*(7599), 361–365, doi:10.1038/nature17190, 2016.

Veedu, D. M., C. Giorgetti, M. Scuderi, S. Barbot, C. Marone, and C. Collettini, Bifurcations at the stability transition of earthquake faulting, *Geophys. Res. Lett.*, *47*(19), e2020GL087,985, doi:10.1029/2020GL087985, 2020.

Wang, L., and S. Barbot, Excitation of San Andreas tremors by thermal instabilities below the seismogenic zone, *Science Advances*, *6*(36), eabb2057, doi:10.1126/sciadv.abb2057, 2020.

Wang, R., F. Martin, and F. Roth, Computation of deformation induced by earthquakes in a multi-layered elastic crust - FORTRAN programs EDGRN/EDCMP, *Comp. Geosci.*, *29*, 195–207, 2003.

Wang, R., F. Lorenzo-Martin, and F. Roth, PSGRN/PSCMP-a new code for calculating co- and post-seismic deformation, geoid and gravity changes based on the viscoelastic-gravitational dislocation theory, *Computers and Geosciences*, *32*, 527–541, 2006.

Weng, H., and J.-P. Ampuero, The dynamics of elongated earthquake ruptures, *J. Geophys. Res.*, *124*(8), 8584–8610, doi:10.1029/2019JB017684, 2019.

Wesnousky, S. G., Predicting the endpoints of earthquake ruptures, *Nature*, *444*(7117), 358–360, doi:10.1038/nature05275, 2006.

Wollherr, S., A.-A. Gabriel, and P. M. Mai, Landers 1992 “reloaded”: Integrative dynamic earthquake rupture modeling, *J. Geophys. Res.*, *124*(7), 6666–6702, 2019.

Wu, Y., and X. Chen, The scale-dependent slip pattern for a uniform fault model obeying the rate-and state-dependent friction law, *J. Geophys. Res.*, *119*(6), 4890–4906, doi:10.1002/2013JB010779, 2014.

Sylvain Barbot
Department of Earth Sciences
University of Southern California
3651 Trousdale Pkwy, Los Angeles, CA 90089, USA.
E-mail: *sbarbot@usc.edu*

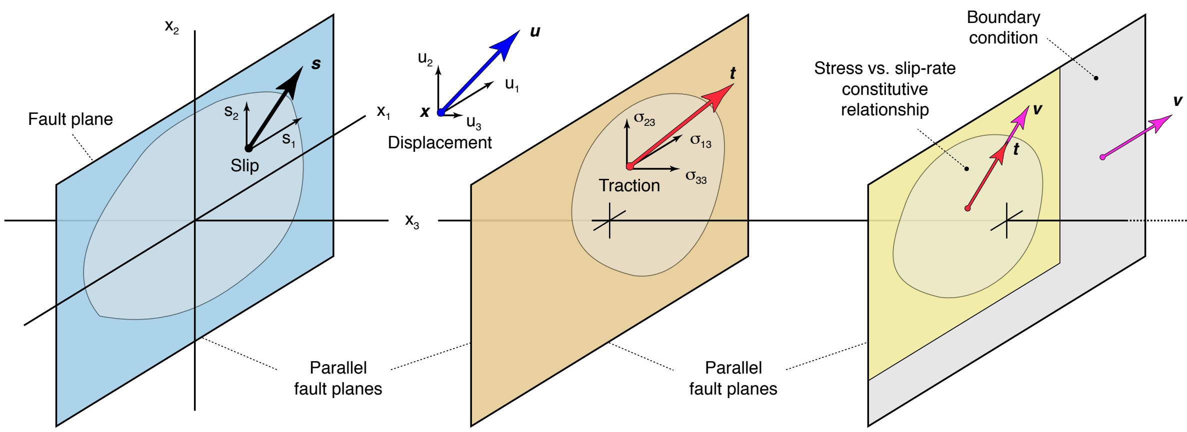

Figure 1: Reference system tied to parallel faults used to express fault slip, displacement, and surface traction. The stress component σ_{33} is positive for extension. Slip corresponds to the displacement offset across a fault. No opening is allowed. A traction/slip-rate constitutive relationship can be used to evaluate seismic-cycle simulations. Some areas of a fault can be subject to velocity boundary conditions to enforce a geological slip-rate or to pin the regions that are permanently locked.

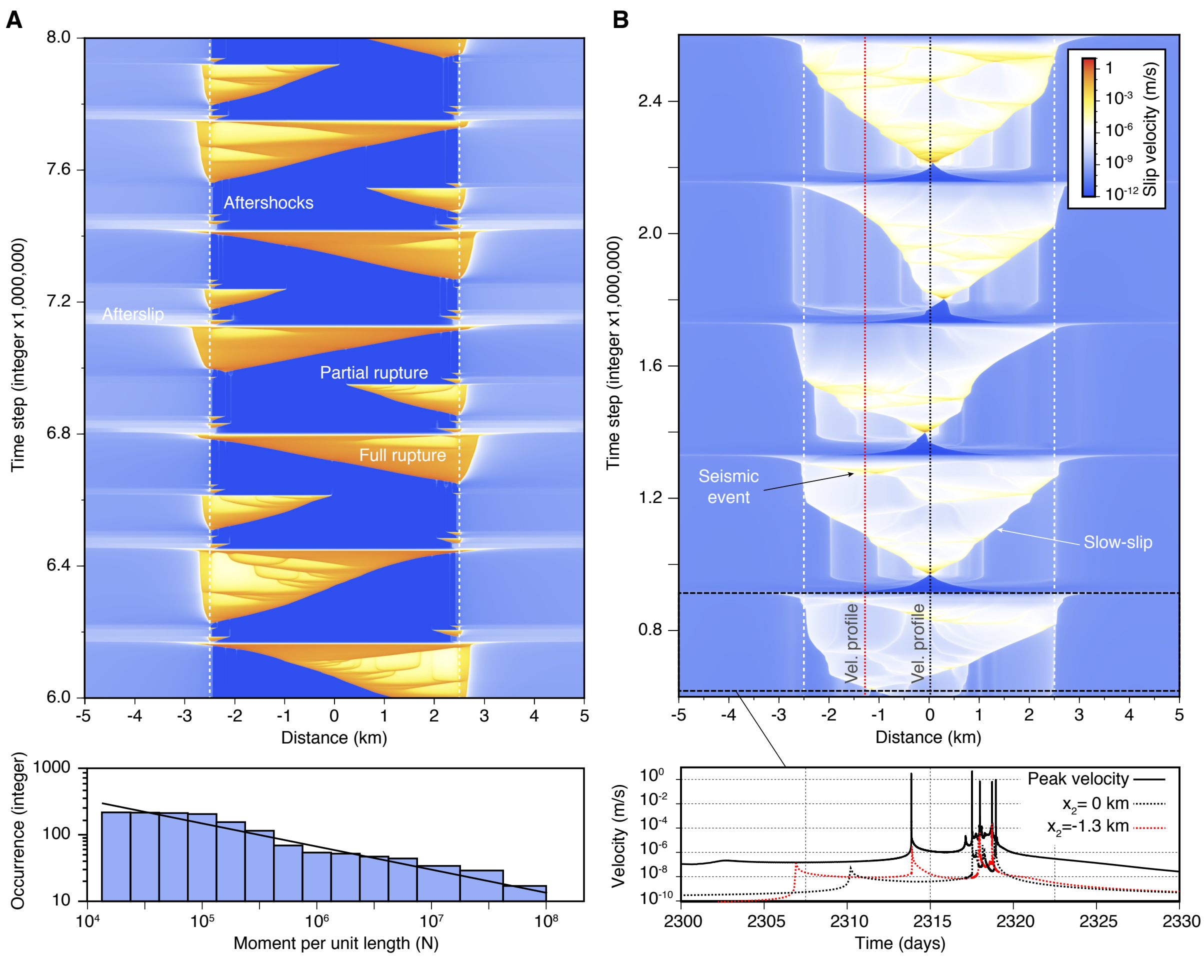

Figure 2: Seismic-cycle simulation of complex slow and fast ruptures in two-dimensional anti-plane strain. A) Fault dynamics for a single fault with $R_u = 266$ and $R_b = 0.285$, with a 300 year aperiodic sequence of full and partial ruptures, including aftershocks in the postseismic period. Bottom) Corresponding distribution of rupture size, approaching that of a power-law (black line, $y \propto 10^{-0.34x}$). B) Cycle of seismogenic slow-slip events with $R_u = 77$ and $R_b = 0.02$ for approximately 20 years. The slow-slip rupture follows multiple fronts that coalesce into short seismic events when they meet. Bottom) Time series of peak velocity (black solid profile), velocity at $x_2 = 0$ (dashed black profile), and at $x_2 = -1.3\,\text{km}$ (dashed red profile) showing the propagation of the creep font over several days and the sudden bursts of seismicity. The velocity-weakening region is marked by white dashed profiles in A and B. The color scale is for both A) and B).

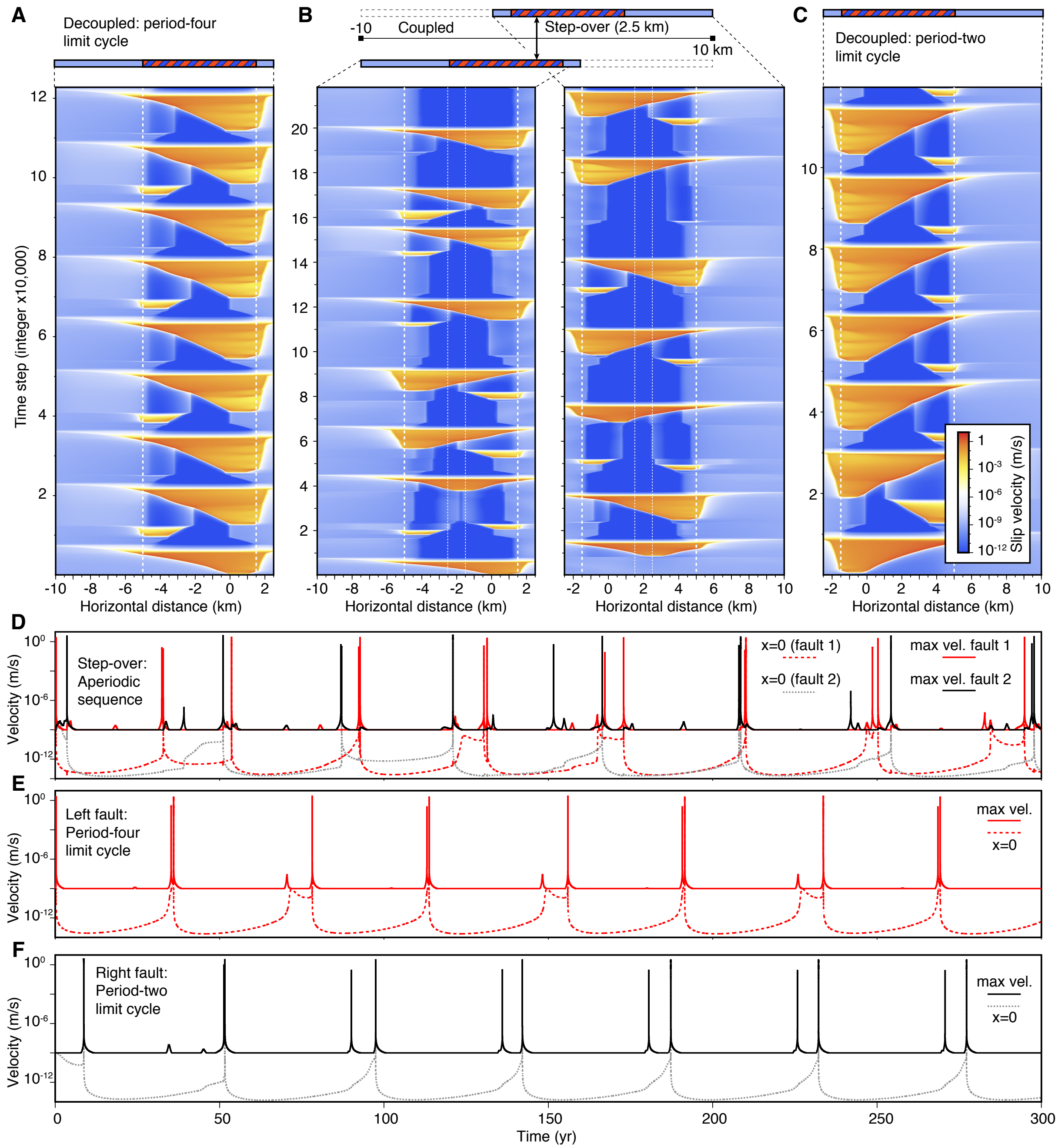

Figure 3: Seismic-cycle simulation of ruptures through a fault step-over with the in-plane strain approximation. A) Fault dynamics of a single fault with $R_u = 17.33$ and $R_b = 0.285$, with period-four cycles of partial and full, slow and fast, ruptures. B) Seismic cycle on the coupled faults in A and C across a 2.5 km step-over showing aperiodic cycles of slow and fast ruptures. The schematic indicates the geometrical arrangement of the two faults, where the dashed rectangles indicate where the faults are pinned in the numerical model. C) Seismic-cycle on a single fault with $R_u = 21.66$ and $R_b = 0.285$ with period-two sequences of partial and full ruptures. D) Time series of fault peak and central velocity for the step-over system. E) Same for fault A in isolation. F) Same for fault B in isolation.

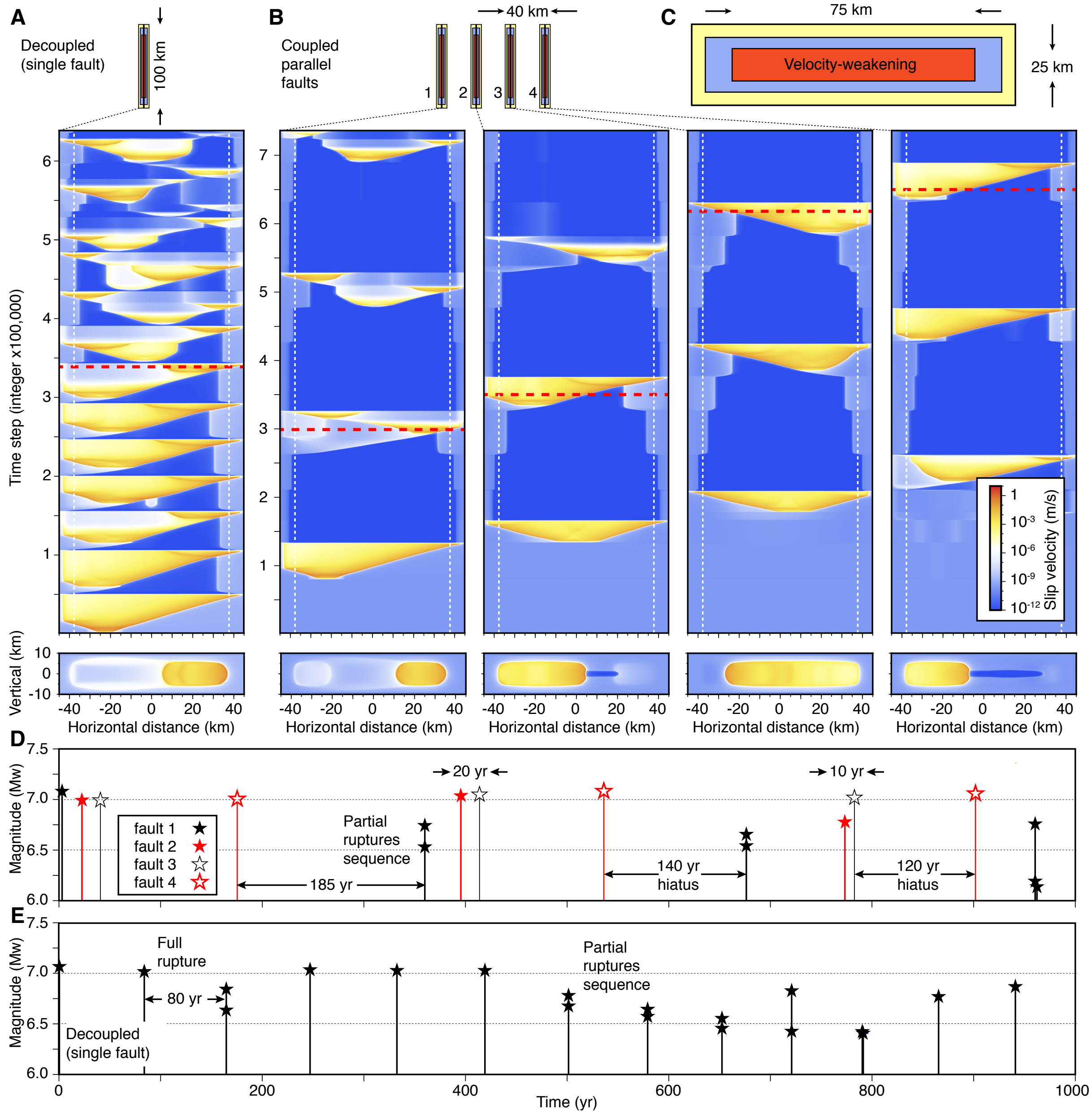

Figure 4: Rupture dynamics on 4 parallel finite faults in three-dimensions. A) Rupture dynamics for a single 100×25 km fault showing semi-period cycles of Mw 6.5 to 7.0 ruptures with 22 partial and full ruptures of the velocity-weakening region within 1000 years. B) Seismic cycle simulation of the coupled dynamics of 4 parallel faults with identical physical properties as fault A, showing 76 seismic events from Mw 5 to 7.0 in the same time period. The velocity field is showed along a profile running across the center of the velocity-weakening region (delineated by white dashed lines). The bottom panels illustrate the rupture process at the time indicated by the dashed red line. C) Dimension of the fault with a 75×25 km velocity-weakening region (red) surrounded by a velocity-strengthening region (blue). A fixed slip rate of 1 nm/s is enforced as a boundary condition in the yellow region. D) Moment magnitude and recurrence time of earthquakes on the four faults in B. E) Same for the single fault A.

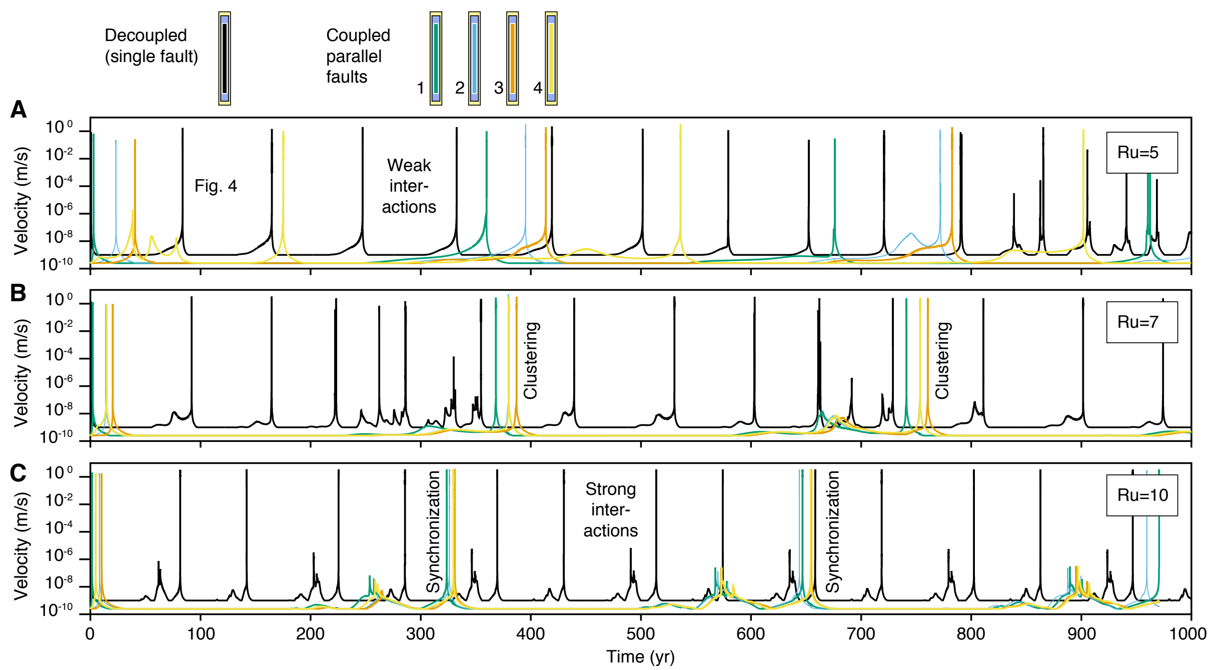

Figure 5: Effect of frictional properties on the degree of seismic synchronicity among parallel faults. A) Peak slip velocity for faults with $R_u = 5$. Detail of this simulation is shown in Figure 4. B) and C) Same for $R_u = 7$ and $R_u = 10$, respectively. The peak velocity for a single, isolated fault with identical physical properties is shown in black. Peak velocity for coupled parallel faults is shown in colors: green for fault 1, light blue for fault 2, orange for fault 3, and yellow for fault 4. Reducing the nucleation size, corresponding to increasing R_u numbers, increasing the degree of mechanical interactions among faults towards seismic clustering and tighter synchronization.